

Accelerated Article Preview

Successful Kinetic Impact into an Asteroid for Planetary Defense

Received: 17 November 2022

Accepted: 8 February 2023

Accelerated Article Preview

Cite this article as: Daly, R. T. et al. Successful Kinetic Impact into an Asteroid for Planetary Defense. *Nature* <https://doi.org/10.1038/s41586-023-05810-5> (2023)

R. Terik Daly, Carolyn M. Ernst, Olivier S. Barnouin, Nancy L. Chabot, Andrew S. Rivkin, Andrew F. Cheng, Elena Y. Adams, Harrison F. Agrusa, Elisabeth D. Abel, Amy L. Alford, Erik I. Asphaug, Justin A. Atchison, Andrew R. Badger, Paul Baki, Ronald-L. Ballouz, Dmitriy L. Bekker, Julie Bellerose, Shyam Bhaskaran, Bonnie J. Buratti, Saverio Cambioni, Michelle H. Chen, Steven R. Chesley, George Chiu, Gareth S. Collins, Matthew W. Cox, Mallory E. DeCoster, Peter S. Ericksen, Raymond C. Espiritu, Alan S. Faber, Tony L. Farnham, Fabio Ferrari, Zachary J. Fletcher, Robert W. Gaskell, Dawn M. Graninger, Musad A. Haque, Patricia A. Harrington-Duff, Sarah Hefter, Isabel Herreros, Masatoshi Hirabayashi, Philip M. Huang, Syau-Yun W. Hsieh, Seth A. Jacobson, Stephen N. Jenkins, Mark A. Jensenius, Jeremy W. John, Martin Jutzi, Tomas Kohout, Timothy O. Krueger, Frank E. Laipert, Norberto R. Lopez, Robert Luther, Alice Lucchetti, Declan M. Mages, Simone Marchi, Anna C. Martin, Maria E. McQuaide, Patrick Michel, Nicholas A. Moskovitz, Ian W. Murphy, Naomi Murdoch, Shantanu P. Naidu, Hari Nair, Michael C. Nolan, Jens Ormö, Maurizio Pajola, Eric E. Palmer, James M. Peachey, Petr Pravec, Sabina D. Raducan, K. T. Ramesh, Joshua R. Ramirez, Edward L. Reynolds, Joshua E. Richman, Colas Q. Robin, Luis M. Rodriguez, Lew M. Roufberg, Brian P. Rush, Carolyn A. Sawyer, Daniel J. Scheeres, Petr Scheirich, Stephen R. Schwartz, Matthew P. Shannon, Brett N. Shapiro, Caitlin E. Shearer, Evan J. Smith, R. Joshua Steele, Jordan K. Steckloff, Angela M. Stickle, Jessica M. Sunshine, Emil A. Superfin, Zahi B. Tarzi, Cristina A. Thomas, Justin R. Thomas, Josep M. Trigo-Rodríguez, B. Teresa Tropic, Andrew T. Vaughan, Dianna Velez, C. Dany Waller, Daniel S. Wilson, Kristin A. Wortman & Yun Zhang

This is a PDF file of a peer-reviewed paper that has been accepted for publication. Although unedited, the content has been subjected to preliminary formatting. Nature is providing this early version of the typeset paper as a service to our authors and readers. The text and figures will undergo copyediting and a proof review before the paper is published in its final form. Please note that during the production process errors may be discovered which could affect the content, and all legal disclaimers apply.

Successful Kinetic Impact into an Asteroid for Planetary Defense

R. Terik Daly*^{†1}
Carolyn M. Ernst*¹
Olivier S. Barnouin*¹
Nancy L. Chabot¹
Andrew S. Rivkin¹
Andrew F. Cheng¹
Elena Y. Adams¹
Harrison F. Agrusa²
Elisabeth D. Abel¹
Amy L. Alford¹
Erik I. Asphaug³
Justin A. Atchison¹
Andrew R. Badger¹
Paul Baki⁴
Ronald-L. Ballouz¹
Dmitriy L. Bekker¹
Julie Bellerose⁵
Shyam Bhaskaran⁵
Bonnie J. Buratti⁵
Saverio Cambioni⁶
Michelle H. Chen¹
Steven R. Chesley⁵
George Chiu¹
Gareth S. Collins⁷
Matthew W. Cox¹
Mallory E. DeCoster¹
Peter S. Ericksen¹
Raymond C. Espiritu¹
Alan S. Faber¹
Tony L. Farnham²
Fabio Ferrari⁸
Zachary J. Fletcher¹
Robert W. Gaskell⁹
Dawn M. Graninger¹
Musad A. Haque¹
Patricia A. Harrington-Duff¹
Sarah Hefter¹
Isabel Herreros¹⁰
Masatoshi Hirabayashi¹¹
Philip M. Huang¹
Syau-Yun W. Hsieh¹
Seth A. Jacobson¹²
Stephen N. Jenkins¹
Mark A. Jensenius¹
Jeremy W. John¹
Martin Jutzi¹³
Tomas Kohout^{14,15}
Timothy O. Krueger¹
Frank E. Laipert^{5‡}
Norberto R. Lopez¹
Robert Luther¹⁶
Alice Lucchetti¹⁷
Declan M. Mages⁵
Simone Marchi¹⁸
Anna C. Martin¹
Maria E. McQuaide¹
Patrick Michel¹⁹
Nicholas A. Moskovitz²⁰
Ian W. Murphy¹
Naomi Murdoch²¹
Shantanu P. Naidu⁵
Hari Nair¹
Michael C. Nolan³
Jens Ormö¹⁰
Maurizio Pajola¹⁷
Eric E. Palmer⁹
James M. Peachey¹
Petr Pravec²²
Sabina D. Raducan¹³
K.T. Ramesh²³
Joshua R. Ramirez¹
Edward L. Reynolds¹
Joshua E. Richman¹
Colas Q. Robin²¹
Luis M. Rodriguez¹
Lew M. Roufberg¹
Brian P. Rush⁵
Carolyn A. Sawyer¹
Daniel J. Scheeres²⁴
Petr Scheirich²²
Stephen R. Schwartz⁹
Matthew P. Shannon¹
Brett N. Shapiro¹
Caitlin E. Shearer¹
Evan J. Smith¹
R. Joshua Steele¹
Jordan K. Steckloff⁹
Angela M. Stickle¹
Jessica M. Sunshine²
Emil A. Superfin¹
Zahi B. Tarzi⁵
Cristina A. Thomas²⁵
Justin R. Thomas¹
Josep M. Trigo-Rodríguez²⁶
B. Teresa Tropic¹
Andrew T. Vaughan⁵
Dianna Velez⁵
C. Dany Waller¹
Daniel S. Wilson¹
Kristin A. Wortman¹
Yun Zhang²

1

2 ¹Johns Hopkins University Applied Physics Laboratory, Laurel, MD, USA

3 ²University of Maryland, College Park, MD, USA

4 ³University of Arizona, Tucson, AZ, USA

5 ⁴Technical University of Kenya, Nairobi, Kenya

- 6 ⁵Jet Propulsion Laboratory, California Institute of Technology, Pasadena, CA, USA
- 7 ⁶Massachusetts Institute of Technology, Cambridge, MA, USA
- 8 ⁷Imperial College, London, UK
- 9 ⁸Politecnico di Milano, Milano, Italy
- 10 ⁹Planetary Science Institute, Tucson, AZ, USA
- 11 ¹⁰Centro de Astrobiología (CAB) CSIC-INTA, Carretera de Ajalvir km4, 28850 Torrejón de
12 Ardoz, Spain
- 13 ¹¹Auburn University, Auburn, AL, USA
- 14 ¹²Michigan State University, East Lansing, MI, USA
- 15 ¹³University of Bern, Bern, Switzerland
- 16 ¹⁴Institute of Geology of the Czech Academy of Sciences, Prague, Czech Republic
- 17 ¹⁵University of Helsinki, Helsinki Finland
- 18 ¹⁶Museum für Naturkunde, Leibniz Institute for Evolution and Biodiversity Science, Berlin,
19 Germany
- 20 ¹⁷INAF-Astronomical Observatory of Padova, Padova, Italy
- 21 ¹⁸Southwest Research Institute, Boulder, CO, USA
- 22 ¹⁹Université Côte d'Azur, Observatoire de la Côte d'Azur, CNRS, Laboratoire Lagrange, Nice,
23 France
- 24 ²⁰Lowell Observatory, Flagstaff, AZ, USA
- 25 ²¹ISAE-SUPAERO, Université de Toulouse, Toulouse, France
- 26 ²²Astronomical Institute AS CR, Ondřejov, Czech Republic
- 27 ²³Johns Hopkins University, Baltimore, MD, USA
- 28 ²⁴University of Colorado, Boulder, CO, USA

29 ²⁵Northern Arizona University, Flagstaff, AZ, USA

30 ²⁶Institute of Space Sciences, Barcelona, Spain

31 *These authors contributed equally to this work.

32 †Corresponding author

33 ‡Currently at Nabla Zero Labs, South Pasadena, CA, USA

34

35 **While no known asteroid poses a threat to Earth for at least the next century, the catalog of**
36 **near-Earth asteroids is incomplete for objects whose impacts would produce regional**
37 **devastation^{1,2}. Several approaches have been proposed to potentially prevent an asteroid**
38 **impact with Earth by deflecting or disrupting an asteroid¹⁻³. A test of kinetic impact**
39 **technology was identified as the highest priority space mission related to asteroid**
40 **mitigation¹. NASA's Double Asteroid Redirection Test (DART) mission is the first full-**
41 **scale test of kinetic impact technology. The mission's target asteroid was Dimorphos, the**
42 **secondary member of the S-type binary near-Earth asteroid (65803) Didymos. This binary**
43 **asteroid system was chosen to enable ground-based telescopes to quantify the asteroid**
44 **deflection caused by DART's impact⁴. While past missions have utilized impactors to**
45 **investigate the properties of small bodies^{5,6}, those earlier missions were not intended to**
46 **deflect their targets and did not achieve measurable deflections. Here we report the DART**
47 **spacecraft's autonomous kinetic impact into Dimorphos and reconstruct the impact event,**
48 **including the timeline leading to impact, the location and nature of the DART impact site,**
49 **and the size and shape of Dimorphos. The successful impact of the DART spacecraft with**
50 **Dimorphos and the resulting change in Dimorphos's orbit⁷ demonstrates that kinetic**
51 **impactor technology is a viable technique to potentially defend Earth if necessary.**

52 The DART spacecraft launched on 24 November 2021. The spacecraft carried a narrow-angle
53 imager called the Didymos Reconnaissance and Asteroid Camera for Optical navigation
54 (DRACO), which was used for optical navigation, terminal guidance, and asteroid
55 characterization⁸. DRACO detected Didymos—the primary asteroid in the binary system—in
56 summed optical navigation images 61 days before impact. On 27 August 2022, 30 days before
57 impact, DRACO began taking optical navigation images of Didymos every five hours, which
58 were processed by the ground optical navigation team⁹.

59
60 On 26 September 2022 at 19:09:24 UTC, four hours and five minutes before impact, the
61 spacecraft's autonomous Small-body Maneuvering Autonomous Real Time Navigation (SMART
62 Nav) system¹⁰ took control of spacecraft navigation (Figure 1a). SMART Nav processed
63 DRACO images onboard¹¹ to identify Didymos, and once resolved, Dimorphos. To achieve
64 impact with Dimorphos, the spacecraft needed to distinguish between the two asteroids and hit
65 the smaller, dimmer one. Due to the dynamics of the binary system and the spatial resolution of
66 DRACO, it was known that the spacecraft's ultimate target—Dimorphos—would be hidden from
67 DRACO's view during most of the autonomous phase. By design, SMART Nav maneuvered the
68 spacecraft towards Didymos until Dimorphos became reliably detected¹⁰. SMART Nav first
69 detected Dimorphos 73 minutes prior to impact, and at 50 minutes prior to impact, SMART Nav
70 began maneuvering towards Dimorphos (Figure 1). As planned, SMART Nav maneuvering
71 ended at 23:11:52 UTC, 2.5 minutes before impact, to give the spacecraft time to settle to
72 minimize jitter and smear in final images. The spacecraft impacted Dimorphos at 23:14:24.183 ±
73 0.004 UTC (see methods). From the start of autonomous navigation until impact, the spacecraft
74 continuously streamed images to the ground, which were immediately broadcast to the public.

75 The final full image was acquired 1.818 seconds before impact and has a pixel scale of 5.5 cm.
76 The final image received on the ground was a partial image acquired 0.855 seconds before
77 impact with a pixel scale of 2.6 cm.
78
79 Little was known about the shape or surface of Dimorphos until DRACO obtained high-
80 resolution images. Ground-based radar observations¹² led to a diameter estimate of 150 ± 30 m.
81 Analysis of telescopic photometric observations yielded a comparable diameter for Dimorphos,
82 171 ± 11 m^{13,14}. Although DRACO imaged only a portion of Dimorphos, and illumination was
83 limited at 60° solar phase, the images were used to construct an asteroid shape model (see
84 methods). The shape model revealed Dimorphos to be an oblate spheroid with a volume-
85 equivalent diameter of 151 ± 5 m (Table 1; Figure 2; Extended Data Fig. 1). Dimorphos's shape is
86 unusual relative to other near-Earth asteroids visited by spacecraft¹⁵⁻¹⁹ and differs from other
87 binary asteroid secondaries observed to date that have measured elongations²⁰⁻²³. However,
88 oblate secondaries show little or no measurable lightcurve amplitude, which biases the
89 observational sample toward elongated secondaries. A new size estimate for Didymos from
90 DRACO images (Table 1) (see methods) combined with previous telescopic observations⁴
91 enables calculation of a more accurate visible ($0.55\ \mu\text{m}$) geometric albedo for the system of 0.15
92 ± 0.02 . This value is on the low side, but within one sigma, of the mean geometric albedo for S-
93 type asteroids²⁴.
94
95 The spacecraft trajectory and pointing were reconstructed to locate the impact site (see methods)
96 (Figure 2). The spacecraft impacted Dimorphos at $8.84 \pm 0.45^\circ$ S, $264.30 \pm 0.47^\circ$ E, within 25 m
97 of the center of the figure, which is very near the scenario for maximizing momentum transfer

98 with an impact through the center of figure²⁵. The one-sigma uncertainty in the impact site
99 location is ± 68 cm (see methods), which is smaller than the size of the spacecraft bus (Figure 3).
100 The impact angle was $73 \pm 7^\circ$ degrees from local horizontal (see methods and Extended Data
101 Fig. 2). The impact site was near two large boulders, labeled boulder 1 (6.5-m long and at its
102 highest point standing ~ 2.2 m above the surrounding terrain; see Extended Data Figure 3) and
103 boulder 2 (6.1-m long and at its highest point standing ~ 1.6 m above the surrounding terrain; see
104 Extended Data Figure 3) in Figure 2b and 2c. The spacecraft approached the asteroid with its
105 solar arrays canted slightly toward the surface (Figure 3). The leading edge of the +Y solar array
106 contacted the surface of boulder 1, and this solar array directly hit boulder 1 (Figure 3). Almost
107 immediately thereafter, the -Y solar array grazed boulder 2, with the leading edge of the -Y array
108 contacting the surface near the base of boulder 2 in downrange direction (Figure 3). Finally, the
109 spacecraft bus hit between boulders 1 and 2 (Figure 3). Although the solar arrays contacted
110 Dimorphos just prior to the spacecraft bus, the bulk of the spacecraft's energy was transferred by
111 the bus, which accounted for $\sim 88\%$ of the spacecraft mass at the time of impact.
112
113 DART images of Dimorphos revealed a boulder-strewn surface (Figure 2a, Extended Data Figs.
114 4 and 5) resembling other small NEAs, such as the S-type (25143) Itokawa¹⁷, and carbonaceous
115 asteroids (101955) Bennu²⁶, and (162173) Ryugu¹⁶, suggesting a rubble-pile structure for
116 Dimorphos. The boulder-rich nature of the surface is apparent in images as coarse as 2–3 m pixel
117 scale (Extended Data Fig. 4). No unambiguous impact crater candidates are observed, which
118 indicates a young surface, though craters can be difficult to identify on boulder-covered
119 terrains^{27–30}. The appearance of Dimorphos contrasts with impressions from lower-resolution

120 images of the Didymos surface, where regional roughness variations are apparent (Extended
121 Data Fig. 4).

122

123 The final complete DRACO image captured a $\sim 880 \text{ m}^2$ area surrounding the impact site at a 5.5-
124 cm pixel scale. The impact region (Figure 2b) exhibits blocky terrain resembling the rest of the
125 observed hemisphere (Figure 2a; Extended Data Fig. 4 and 5). There is evidence for variation
126 within boulders, “rocks on rocks” similar to observations on Bennu³¹, and partially buried
127 boulders (Extended Data Fig. 5). The longest axes of boulders counted in the final complete
128 image are 0.16 m to 6.5 m in length. The impact region has fewer boulders in the 0.2–0.5 m size
129 range than expected if the cumulative distribution followed a single power-law, even though the
130 pixel scale of the image is sufficient for their identification (Extended Data Fig. 6). There is no
131 evidence for expansive smooth deposits (grain size smaller than the image pixel scale) such as
132 those seen on Itokawa¹⁷. The blocky nature of the impact site likely influenced crater formation,
133 ejecta, and momentum enhancement, as seen in impact experiments^{28,32–34}, numerical
134 simulations^{25,35}, and the Small Carry-on Impactor experiment on Hayabusa2⁵.

Table 1. Properties of the DART impact, Dimorphos, and Didymos.

Time of impact	26 September 2022 at 23:14:24.183 ± 0.004 UTC
Impact speed (km/s)	6.1449 ± 0.0003
Impact angle (degrees)	73 ± 7 from local horizontal, 17 ± 7 from the surface normal
Impact site location (latitude, longitude)	8.84 ± 0.45° S, 264.30 ± 0.47° E
Impact site offset from center of figure (m)	25 ± 1
Spacecraft mass at time of impact (kg)	579.4 ± 0.7
Impact kinetic energy (GJ)	10.94 ± 0.01
Extent of Dimorphos (m)	X: 177 ± 2 Y: 174 ± 4 Z: 116 ± 2
Extent of Didymos (m)	X: 849 ± 15 Y: 851 ± 15 Z: 620 ± 15
Volume of Dimorphos (km ³)	0.00181 ± 10%
Diameter of volume-equivalent sphere for Dimorphos (m)*	151 ± 5
Diameter of volume-equivalent sphere for Didymos (m)*	761 ± 26
Mass of the Didymos system (kg)	(5.6 ± 0.5) × 10 ¹¹
Density of Didymos system (kg/m ³)	2400 ± 300
Inferred Mass of Dimorphos (kg)	4.3 × 10 ⁹

136 *Computed from the volumes of the shape models, not the volumes of triaxial ellipsoids
 137 with the extents listed above.

139 DART did not measure the mass of Dimorphos. Instead, Dimorphos's mass is estimated using
140 the orbital properties of the binary system, the total volume of the system, and an assumption that
141 Didymos and Dimorphos have equal bulk densities (see methods). This assumption cannot be
142 rigorously tested from DART data, but this approach leads to a bulk density of Dimorphos of
143 2400 kg/m^3 (Table 1) with difficult-to-quantify uncertainties.

144
145 Based on analyses of reflectance spectra, the best meteoritic analogs for Didymos are L and LL
146 chondrites^{36,37}. L and LL chondrites have grain densities³⁸ of $3580 \pm 10 \text{ kg/m}^3$ and $3520 \pm$
147 10 kg/m^3 , respectively. If one assumes Dimorphos has the same composition as Didymos and
148 that these meteorite values represent the grain density of Dimorphos, then a bulk density of
149 $\sim 2400 \text{ kg/m}^3$ implies a Dimorphos bulk porosity of order 30% (with a difficult-to-quantify
150 uncertainty; see methods). This level of bulk porosity is not inconsistent with a rubble-pile
151 structure for Dimorphos, a structure suggested by the boulder-rich character of Dimorphos's
152 surface. This bulk porosity likely exists as a combination of macroporosity between pieces of
153 rubble and microporosity within individual pieces of rubble. L and LL chondrite samples have
154 porosities of $8.0 \pm 0.3\%$ and $9.5 \pm 0.6\%$, respectively³⁸, which would imply that macroporosity is
155 substantial on Dimorphos. Estimates of the density and porosity of Dimorphos will be
156 significantly improved when ESA's Hera mission arrives at the Didymos system in early 2027³⁹.

157
158 DART's successful autonomous targeting of a small asteroid with limited prior knowledge is a
159 key first accomplishment on the path to advancing kinetic impactor technology to an operational
160 capability. DART's impact indicates that a precursor reconnaissance mission is not a prerequisite
161 for intercepting a sub-kilometer asteroid, though the characterization done by a precursor

162 mission would provide valuable information for optimizing, planning and predicting the outcome
163 with greater certainty. Kinetic impactor technology for asteroid deflection requires having
164 sufficient warning time—at least several years but preferably decades—to prevent an asteroid
165 impact with the Earth¹⁻³. Nevertheless, this first successful step to demonstrate the viability of
166 kinetic impactor technology for planetary defense builds optimism about humanity’s capacity to
167 protect the Earth from an asteroid threat.

168

169 **References**

- 170 1. *Defending Planet Earth: Near-Earth Object Surveys and Hazard Mitigation Strategies*. 12842
171 (National Academies Press, 2010). doi:10.17226/12842.
- 172 2. Interagency Working Group for Detecting and Mitigating the Impact of Earth-bound Near-
173 Earth Objects. National Near-Earth Object Preparedness Strategy and Action Plan. (2018).
- 174 3. Committee on the Planetary Science and Astrobiology Decadal Survey, Space Studies Board,
175 Division on Engineering and Physical Sciences, & National Academies of Sciences,
176 Engineering, and Medicine. *Origins, Worlds, and Life: A Decadal Strategy for Planetary
177 Science and Astrobiology 2023-2032*. 26522 (National Academies Press, 2022).
178 doi:10.17226/26522.
- 179 4. Rivkin, A. S. et al. *The Double Asteroid Redirection Test (DART): Planetary Defense
180 Investigations and Requirements*. *Planet. Sci. J.* **2**, 173 (2021).
- 181 5. A’Hearn, M. F. et al. Deep impact: excavating comet Tempel 1. *science* **310**, 258–264 (2005).
- 182 6. Arakawa, M. et al. An artificial impact on the asteroid (162173) Ryugu formed a crater in the
183 gravity-dominated regime. *Science* **368**, 67–71 (2020).

- 184 7. Thomas, C. A. Orbital Period Change of Dimorphos Due to the DART Kinetic Impact. *Nature*
185 **(this issue)**, (2022).
- 186 8. Fletcher, Z. J. *et al.* Didymos Reconnaissance and Asteroid Camera for OpNav (DRACO):
187 design, fabrication, test, and operation. in *Space Telescopes and Instrumentation 2022: Optical,*
188 *Infrared, and Millimeter Wave* (eds. Coyle, L. E., Perrin, M. D. & Matsuura, S.) 11 (SPIE,
189 2022). doi:10.1117/12.2627873.
- 190 9. Rush, B. P. *et al.* Optical Navigation for the DART Mission. in *33rd AAS/AIAA Space Flight*
191 *Mechanics Meeting*, Austin TX, 15–19, January 2023 (AAS 23-234).
- 192 10. Adams, E. *et al.* Double Asteroid Redirection Test: The Earth Strikes Back. in *2019 IEEE*
193 *Aerospace Conference* 1–11 (IEEE, 2019). doi:10.1109/AERO.2019.8742007.
- 194 11. Bekker, D., Smith, R. & Tran, M. Q. Guiding DART to Impact — the FPGA SoC Design of
195 the DRACO Image Processing Pipeline. in *2021 IEEE Space Computing Conference (SCC)*
196 122–133 (IEEE, 2021). doi:10.1109/SCC49971.2021.00020.
- 197 12. Naidu, S. P. *et al.* Radar observations and a physical model of binary near-Earth asteroid 65803
198 Didymos, target of the DART mission. *Icarus* **348**, 113777 (2020).
- 199 13. Pravec, P. *et al.* Photometric Observations of the Binary Near-Earth Asteroid (65803) Didymos
200 in 2015–2021 Prior to DART Impact. *Planet. Sci. J.* **3**, 175 (2022).
- 201 14. Scheirich, P. & Pravec, P. Preimpact Mutual Orbit of the DART Target Binary Asteroid
202 (65803) Didymos Derived from Observations of Mutual Events in 2003–2021. *Planet. Sci. J.* **3**,
203 163 (2022).
- 204 15. Zuber, M. T. *et al.* The Shape of 433 Eros from the NEAR-Shoemaker Laser Rangefinder.
205 *Science* **289**, 2097–2101 (2000).

- 206 16. Watanabe, S. *et al.* Hayabusa2 arrives at the carbonaceous asteroid 162173 Ryugu—A
207 spinning top-shaped rubble pile. *Science* **364**, 268–272 (2019).
- 208 17. Fujiwara, A. *et al.* The Rubble-Pile Asteroid Itokawa as Observed by Hayabusa. *Science* **312**,
209 1330–1334 (2006).
- 210 18. Huang, J. *et al.* The Ginger-shaped Asteroid 4179 Toutatis: New Observations from a
211 Successful Flyby of Chang’e-2. *Sci. Rep.* **3**, 3411 (2013).
- 212 19. Barnouin, O. S. *et al.* Shape of (101955) Bennu indicative of a rubble pile with internal
213 stiffness. *Nat. Geosci.* **12**, 247–252 (2019).
- 214 20. Ostro, Steven. J. *et al.* Radar Imaging of Binary Near-Earth Asteroid (66391) 1999 KW4.
215 *Science* **314**, 1276–1280 (2006).
- 216 21. Becker, T. M. *et al.* Physical modeling of triple near-Earth Asteroid (153591) 2001 SN263
217 from radar and optical light curve observations. *Icarus* **248**, 499–515 (2015).
- 218 22. Naidu, S. P. *et al.* RADAR IMAGING AND CHARACTERIZATION OF THE BINARY
219 NEAR-EARTH ASTEROID (185851) 2000 DP107. *Astron. J.* **150**, 54 (2015).
- 220 23. Pravec, P. *et al.* Binary asteroid population. 3. Secondary rotations and elongations. *Icarus* **267**,
221 267–295 (2016).
- 222 24. Pravec, P., Harris, A. W., Kušnirák, P., Galád, A. & Hornoch, K. Absolute magnitudes of
223 asteroids and a revision of asteroid albedo estimates from WISE thermal observations. *Icarus*
224 **221**, 365–387 (2012).
- 225 25. Stickle, A. M. *et al.* Effects of Impact and Target Parameters on the Results of a Kinetic
226 Impactor: Predictions for the Double Asteroid Redirection Test (DART) Mission. *Planet. Sci.*
227 *J.* **3**, 248 (2022).

- 228 26. Lauretta, D. S. *et al.* The unexpected surface of asteroid (101955) Bennu. *Nature* **568**, 55–60
229 (2019).
- 230 27. Hirata, N. *et al.* A survey of possible impact structures on 25143 Itokawa. *Icarus* **200**, 486–502
231 (2009).
- 232 28. Barnouin, O. S., Daly, R. T., Cintala, M. J. & Crawford, D. A. Impacts into coarse-grained
233 spheres at moderate impact velocities: Implications for cratering on asteroids and planets.
234 *Icarus* **325**, 67–83 (2019).
- 235 29. Hirata, N. *et al.* The spatial distribution of impact craters on Ryugu. *Icarus* **338**, 113527
236 (2020).
- 237 30. Daly, R. T. *et al.* The Morphometry of Impact Craters on Bennu. *Geophys. Res. Lett.* **47**,
238 (2020).
- 239 31. Jawin, E. R. *et al.* Global Patterns of Recent Mass Movement on Asteroid (101955) Bennu. *J.*
240 *Geophys. Res. Planets* **125**, (2020).
- 241 32. Tatsumi, E. & Sugita, S. Cratering efficiency on coarse-grain targets: Implications for the
242 dynamical evolution of asteroid 25143 Itokawa. *Icarus* **300**, 227–248 (2018).
- 243 33. Okawa, H. *et al.* Effect of boulder size on ejecta velocity scaling law for cratering and its
244 implication for formation of tiny asteroids. *Icarus* **387**, 115212 (2022).
- 245 34. Ormö, J. *et al.* Boulder exhumation and segregation by impacts on rubble-pile asteroids. *Earth*
246 *Planet. Sci. Lett.* **594**, 117713 (2022).
- 247 35. Raducan, S. D., Jutzi, M., Zhang, Y., Ormö, J. & Michel, P. Reshaping and ejection processes
248 on rubble-pile asteroids from impacts. *Astron. Astrophys.* **665**, L10 (2022).
- 249 36. de León, J., Licandro, J., Duffard, R. & Serra-Ricart, M. Spectral analysis and mineralogical
250 characterization of 11 olivine–pyroxene rich NEAs. *Adv. Space Res.* **37**, 178–183 (2006).

251 37. Dunn, T. L., Burbine, T. H., Bottke, W. F. & Clark, J. P. Mineralogies and source regions of
252 near-Earth asteroids. *Icarus* **222**, 273–282 (2013).

253 38. Flynn, G. J., Consolmagno, G. J., Brown, P. & Macke, R. J. Physical properties of the stone
254 meteorites: Implications for the properties of their parent bodies. *Geochemistry* **78**, 269–298
255 (2018).

256 39. Michel, P. *et al.* The ESA Hera Mission: Detailed Characterization of the DART Impact
257 Outcome and of the Binary Asteroid (65803) Didymos. *Planet. Sci. J.* **3**, 160 (2022).

258

259 **Figure Captions**

260 **Figure 1. Milestones leading to impact with Dimorphos from the time SMART Nav began**
261 **targeting until the end of SMART Nav maneuvering.** Each column corresponds to a
262 milestone. Each row shows, from top to bottom, the raw DRACO image at the time of that
263 milestone with circles indicating the two asteroids detected by onboard processing and identified
264 by SMART Nav (yellow dashed circles, Didymos; green solid circles, Dimorphos), a zoom-in of
265 Didymos, and a zoom-in of Dimorphos. The SMART Nav system used information in DRACO
266 images to successfully impact Dimorphos. In all images, Dimorphos north pole (+Z) is toward
267 the bottom left. Images from left to right: dart_0401915351_36903_01_raw.fits,
268 dart_0401925635_06853_01_raw.fits, dart_0401927052_23729_01_raw.fits, and
269 dart_0401929899_33346_01_raw.fits.

270

271 **Figure 2. The asteroid Dimorphos and the DART impact site as seen in calibrated DRACO**
272 **images.** (a) Dimorphos with an appropriately scaled and correctly oriented outline of the DART
273 spacecraft centered on the impact site. Note the size of the spacecraft relative to the asteroid. The

274 spacecraft bus was approximately 1.2 x 1.3 x 1.3 meters from which other structures extended,
275 resulting in dimensions of approximately 1.8 x 1.9 x 2.6 meters. The spacecraft also had two
276 large solar arrays that were each 8.5 meters long. (b) A closer view of the DART impact site
277 showing the outline of the spacecraft bus and solar arrays over the DRACO image. Note the
278 positions of the two solar arrays relative to two large boulders, labeled 1 (6.5 m long) and 2
279 (6.1 m long). This subframe is from an image taken 2.781 seconds before impact. (c) The
280 spacecraft bus hit between boulders 1 and 2, whereas the solar arrays interacted with these
281 boulders. This subframe is from an image taken 1.818 seconds before impact. The arrow at the
282 lower left of panel (a) indicates the direction of Dimorphos +Z (N) axis. The solid white box in
283 (a) shows the location of the image in (b). The dashed gray box in (b) shows the location of the
284 image in (c). Panels (b) and (c) show subimages of the full frame. Image names: (a)
285 dart_0401930039_14119_01_iof.fits, (b) dart_0401930048_45552_01_iof.fits, (c)
286 dart_0401930049_43695_01_iof.fits.

287
288 **Figure 3. Relationship between the spacecraft and topography at the DART impact site.** (a)
289 – (c) show the position of the spacecraft immediately before the impact of the spacecraft bus
290 from different perspectives to visualize the three-dimensional interactions between the spacecraft
291 and surface. In panel (a), Dimorphos north is toward the top of the panel. In panel (b) Dimorphos
292 north is to the right. In panel (c) Dimorphos north is roughly into the page. In all panels, -Y solar
293 array points to Dimorphos north. Length scales vary in these perspective views; the scale bars
294 shown are approximate. Boulders 1 and 2 correspond to boulders 1 and 2 in Figure 2. The
295 caption to Figure 2 gives the spacecraft dimensions.

296

297 **Methods**

298 **Determining the time of impact**

299 The time of impact was computed from spacecraft clock timestamps inserted into each
300 downlinked telemetry frame by the spacecraft's radio. A new telemetry frame was produced
301 every 2.9853 milliseconds with a precision of 20 microseconds. Assuming the impact occurred
302 in the middle of the frame after the final received frame placed the time of impact to within \pm
303 half a frame period:

304 $401,930,051.59326 \pm 0.00149$ s spacecraft clock time

305 This spacecraft clock time of impact was converted to UTC. This conversion increases the
306 uncertainty slightly:

307 $2022-26-9\ 23:14:24.183 \pm 0.004$ s UTC

308 This time is the UTC of the impact at Dimorphos, not the time on Earth when the last telemetry
309 frame was received. As each DRACO image is timestamped with a spacecraft clock value, the
310 time to impact for each image can be computed with similar accuracy.

311

312 **Shape modeling of Dimorphos**

313 We built the shape model using stereophotoclinometry (SPC), a technique that has been widely
314 used to model the shape of small bodies⁴⁰⁻⁴². Prior to DART's impact, the shape modeling team
315 conducted tests to understand the strengths and limitations of the SPC approach given the data
316 expected from DART⁴³. DART images pose a challenge for any image-based shape modeling
317 technique due to the single viewing geometry and lighting condition. SPC provides robust results
318 despite these challenges⁴³.

319

320 Extended Data Fig. 7 illustrates the steps used to build the Dimorphos shape model. First, we
321 used DRACO images to determine the dimensions of an initial triaxial ellipsoid. The ellipsoid
322 was constrained by the location of the sunlit limb, the location of the limb lit by light scattered
323 off Didymos, and the position of the terminator. Together, the sunlit and Didymos-lit limbs
324 revealed the complete extents of the X and Z axes of Dimorphos (Extended Data Fig. 8). The
325 position of the terminator constrained the Y-axis extent. The last DRACO image to contain all of
326 Dimorphos in the field of view was registered to the ellipsoid. Other DRACO images were
327 registered to that image or, in the case of the highest-resolution images of the impact site, to the
328 immediately preceding image. In order to correctly determine the scale of the shape model, we
329 used the known time of impact and spacecraft speed to set the spacecraft range for each image.
330

331 Next, we pursued parallel paths (Extended Data Fig. 7). The first path used standard SPC
332 processes to construct small digital terrain models (called “maplets”) using an SPC program
333 called lithos^{40,42,43}. Maplets were tiled all across the surface of the asteroid in the areas seen by
334 DRACO. Maplets went through several iterations to compute the maplet topography^{40,42,43}. After
335 several iterations, the maplet ensemble was averaged to create a global digital terrain model
336 (DTM). Areas without maplet coverage remained unchanged. This cycle was repeated with
337 maplets of increasingly finer ground-sample distances (GSD) in the areas covered by higher-
338 resolution images surrounding the impact site. The finest-scale maplets had a GSD of 3 cm,
339 comparable to the pixel scale of the final, partial DRACO image. The second path focused on
340 matching the sunlit limb. We built maplets along the sunlit limb that were conditioned by limb
341 points identified in the tilt-to-height integration in an SPC iteration. These maplets were made at
342 only two ground-sample distances due to the coarser resolution of images that contained limb.

343 Once the topography in the standard maplets and limb-only maplets stabilized, we united them
344 via several SPC iterations and proceeded to build the global DTM.

345
346 The areas covered by maplets on Dimorphos global DTM are shown in Extended Data Fig. 1 as
347 shaded gray regions. The blue and magenta points show the locations of the sunlit and Didymos-
348 lit limbs. The unseen side of the asteroid is roughly centered on the 90° East view. The shape
349 model has the volume and extents reported in Table 1. The global DTM has a typical GSD of
350 26 centimeters, but that resolution is only meaningful in the areas covered by maplets.

351 We also used the standard maplets to construct a DTM of the impact site. The impact site is
352 covered by the highest-resolution images, so the impact site can support finer-scale topography
353 than the global model. The impact site DTM has a GSD of 5 cm and is shown in Figure 3.

354
355 Due to the short period of time for which we have resolved images of Dimorphos, the rotation
356 pole, prime meridian, and rotation rate of Dimorphos could not be updated using SPC. Instead,
357 we used values derived by ground-based observers. In the equatorial J2000 frame, the pole
358 values used for Dimorphos are¹⁴:

359 BODY120065803_POLE_RA = (60.936309840897856, 0, 0)

360 BODY120065803_POLE_DEC = (-71.674565992873852, 0, 0)

361

362 The coordinate system of the global DTM of Dimorphos has the prime meridian pointed toward
363 Didymos, consistent with IAU convention:

364 BODY120065803_PM = (64.914870949788195, 724.723943017441570,

365 1.0840372309e-06)

366 A planetary constants kernel (PCK) with these values is available at
367 https://ssd.jpl.nasa.gov/ftp/eph/small_bodies/dart/dimorphos/archive/ called “dimorphos_s501-
368 preimp.tpc”. Documentation for PCK files, including units for the terms listed above, is available
369 here:
370 https://naif.jpl.nasa.gov/pub/naif/toolkit_docs/FORTRAN/req/pck.html#Text%20PCK%20Kernel%20Variable%20Names. Dimorphos's north pole is in the +Z direction of the shape model but
372 oriented toward ecliptic south.

373

374 **Shape model uncertainties**

375 We quantified uncertainties in the global DTM of Dimorphos using techniques employed to
376 estimate the uncertainties associated with the global DTM of Bennu⁴⁴. These techniques were
377 also used to assess uncertainties in shape models developed during pre-impact tests done for
378 DART⁴³. The analyses involved comparing DRACO images against the global DTM when
379 rendered with the same lighting and viewing geometry as the image. We used three analyses
380 described in the above references. The first method, referred to as the limb/terminator method,
381 used image thresholding to identify limb and terminator in the DRACO image and rendered
382 shape model. The thresholded images were subtracted to reveal mismatches between the image
383 and rendered shape model and any size bias in the model (Extended Data Fig. 9a-9e). The second
384 and third methods relied on analysis of corresponding surface features, or keypoints, in images
385 and the rendered shape model, to understand errors in the overall size of the shape model
386 (Extended Data Fig. 9f-9i). In the second method, referred to as keypoint matching, the rendered
387 image was rotated, translated, and scaled to minimize differences in keypoint locations on the
388 DRACO image and rendered shape model. The third method, referred to as keypoint distance,

389 was based on the measured distances between all keypoints in the DRACO image and rendered
390 shape model.

391
392 The limb/terminator assessments indicated that the model is 75 cm too small in X, Y, and Z, with
393 a limb uncertainty of 1.3 – 2 m. Most of the mismatch between DRACO images and the rendered
394 shape model occurred along the limb and terminator. We expected larger uncertainties in these
395 areas due to the limited coverage and single lighting condition in DRACO images. The keypoints
396 indicated that the Dimorphos shape model is 6 ± 29 cm too large and that features in the model
397 have point-separation errors of -11 ± 20 cm. The keypoint assessments indicated that the model
398 performed well in areas where DRACO resolved detailed surface features, which is the area of
399 the model that is most relevant to understanding the topography of the impact site. Comparisons
400 between shadow lengths in DRACO images and shadow lengths in shape model renderings
401 indicated that some boulder heights are too small. This mismatch was expected based on shape
402 modeling tests done for DART and is a consequence of constructing the shape model from a
403 single lighting condition and viewing geometry⁴³. Shadow lengths suggest that height of boulder
404 1 in the impact site DTM is $\sim 10\%$ too small, but the height of boulder 2 in the impact site DTM
405 is correct. Based on all of these analyses, we assumed uncertainties of two meters in the extents
406 of Dimorphos in the X and Z directions.

407
408 Because DRACO saw a complete outline of the asteroid (Extended Data Figure 8) and the
409 spacecraft approach geometry was such that this outline was primarily in the X-Z plane, the
410 shape model dimension uncertainties in X and Z are less than 1% (Table 1). Hence, the Y-axis
411 extent is the largest source of uncertainty in the volume. Future work will refine the errors in the

412 Y-axis, but for the time being we assume the uncertainty in Y is two times the uncertainties in X
413 and Z (i.e., 4 meters).

414

415 Measuring the volume of Dimorphos and realistically estimating uncertainties on that quantity is
416 of particular interest because it directly affects our understanding of the mass of the asteroid. In
417 the shape modeling tests⁴³, we took scaled shape models of an ellipsoid, Itokawa, and Bennu,
418 rendered a set of simulated DRACO images from the “truth” shape models, and then used SPC
419 to build shape models from simulated images⁴³. We compared the volumes of the models built
420 using SPC against the volumes of truth models⁴³. The volume errors in those tests ranged from -
421 2% to +23%⁴³. The test with the lowest volume error was for an ellipsoidal asteroid. The
422 roughly ellipsoidal shape of Dimorphos as seen by DRACO suggests that the volume error in the
423 Dimorphos global DTM is likely on the order of several percent, rather than 23%, by virtue of
424 the simplicity of Dimorphos’s long-wavelength shape. Moreover, in the tests with the largest
425 volume errors, the terminator of the shape model—which is the primary constraint on the extent
426 of the shape into and out of the page—did not match the terminator of the original images. In the
427 case of Dimorphos, the terminator matched nicely between the global DTM and the rendered
428 shape model (Extended Data Figure 9). Given the results from the shape modeling tests⁴³, this
429 agreement indicated that the volume errors for Dimorphos are likely on the order of several
430 percent. Based on these assessments, a volume error of 5% seems probable. But, we adopted a
431 volume uncertainty of 10% to be conservative. This volume error is larger than the value implied
432 by the reported uncertainties in the X, Y, and Z extents, but the intent is to be conservative.

433

434

435 **Shape modeling of Didymos**

436 A preliminary SPC shape model of Didymos was built from DRACO data. This model led to the
437 preliminary volume and extent of Didymos reported in Table 1. DRACO images revealed a
438 smaller Z-axis and showed that the visible portion of the X-axis likely needs to be extended by a
439 few tens of meters compared to a radar-derived shape model¹². We used the techniques
440 employed to estimate shape model uncertainties described in the “Shape modeling of
441 Dimorphos” section to assess the preliminary SPC shape model of Didymos. Because the full X-
442 and Z-extents of Didymos cannot be measured in DRACO images (in contrast to Dimorphos),
443 we conservatively attributed an uncertainty of 15 m to the lengths of all the axes of Didymos.

445 **Impact site identification**

446 The construction of an SPC shape model produced a set of surface landmarks that were used to
447 determine the location (at the time of each image) of the spacecraft relative to the surface in the
448 Dimorphos body fixed frame. This procedure used the spacecraft’s Didymos relative velocity
449 computed by the ground navigation team using a combination of radiometric tracking data
450 (Doppler, range) and optical images of Didymos. We used this information and the shape model
451 of Dimorphos to compute the location of the impact site. The positions of the DART spacecraft
452 from SPC were converted to the inertial J2000 frame and corrected for light time and aberration.
453 The velocity of the spacecraft was estimated by fitting a second-order polynomial function to
454 these positions as a function of time. This approach is identical to that employed previously⁴⁵ to
455 estimate the position of the Hayabusa spacecraft relative to Itokawa. We used the locations from
456 the last 14 complete images collected by DART to determine the spacecraft velocity. These
457 images contained large numbers of landmarks due to their fine pixel scales, which help anchor

458 the spacecraft position for each image. The fit residuals (i.e., the difference between the fit of the
459 spacecraft location to that determined from SPC) are $< 1\text{ m}$ (Extended Data Figure 10).

460

461 We combined our estimated velocity and the SPC-derived spacecraft positions of the last five
462 images to determine the impact location. Only the last five images were used to locate the impact
463 because heater cycling on the spacecraft introduced cyclic error rates in the inertial attitude
464 knowledge. These rates were estimated to be small at the time of impact due to the timing of
465 impact relative to heater cycling but at their highest approximately 30 seconds prior to impact.
466 Using only the last few images reduced the influence of this known (and cumulative) error
467 source. At each of these five spacecraft positions, we propagated the velocity vector until it
468 intersected with the surface of the Dimorphos shape model. We took the mean of these positions
469 as the impact location. We also computed the spacecraft state at a few different heights above the
470 intersection point in order to determine the order in which the solar arrays and bus contacted the
471 surface. The propagation from each of the last five images provided the same impact point to
472 within 1 cm. The uncertainties in the impact point location (reported in Table 1) are dominated
473 by the residuals to the fits of the spacecraft position obtained by SPC in the Y and Z directions
474 (Extended Data Figure 10).

475

476 **Impact angle assessments**

477 The tilt angle of the surface relative to the impact velocity vector defines the impact angle.

478 Because the impact site DTM resolves topography at a 5-cm GSD, the spacecraft bus would have
479 interacted with on the order of a thousand facets of the DTM. Therefore, we calculated a mean
480 tilt with respect to the impact velocity vector for each facet in the impact site DTM. The mean

481 tilt calculation is based on previous work⁴¹; however, we computed mean tilt with respect to the
482 impact velocity vector, v , rather than the radial vector to a given facet to determine the impact
483 angle.

484
485 The magnitude of the mean tilt for a facet at the impact point is the angle between v and the
486 average normal, n_{av} , which is the weighted average of the normal vectors of all facets in the user-
487 defined region, $n_{av} = \sum(n_i A_i) / \sum A_i$ surrounding the impact point. In this study, this region was
488 1.5 m in radius in order to exceed the size of the spacecraft bus. The normal vector of each facet
489 in the region of interest, n_i , was weighted by A_i , the area of the facet projected onto a best-fit
490 plane to the region selected to determine the surface tilt. This yields a mean tilt = $\arccos(n_{av} \cdot v$
491 $/ |n_{av}| |v|)$. Impact angle, θ , which is typically defined relative to the local horizontal for planetary
492 impacts, is given by $\theta = 90 - (\text{mean tilt})$. The impact angle shown in Table 1 is computed from the
493 mean tilt and θ of the facet closest to the impact point.

494
495 As discussed in the “Impact site identification” section, the location of the impact site has an
496 uncertainty of ± 68 cm. To understand the range of mean tilts that DART may have encountered
497 given the uncertainty in the impact location, we considered the distribution of mean tilt for all
498 facets within a circle with radius 68 cm centered on the impact site (Extended Data Figure 2).
499 The standard deviation of this distribution was 7° (one sigma), which we attributed as the
500 uncertainty of the impact angle DART may have experienced.

501

502 **Boulder Counting**

503 The longest axis of each boulder in the final full DRACO image was identified as a line (as done
504 for asteroid (101955) Bennu⁴⁶. The length of the longest axis was determined from the line length
505 and image pixel scale, assuming the last full image as a “flat” scene. The total number of boulders
506 and pebbles identified in the final full DRACO image impact site is 953 and range in size (that is,
507 length of the longest axis) from 0.16 (limit of image resolution, assuming ≥ 3 pixel sampling⁴⁷) to
508 6.5 m. The resulting size–frequency distribution is presented in Extended Data Figure 6.

509 **Estimates for the density of Dimorphos**

511 To first order, the combined system mass, M_{sys} , was estimated using Kepler’s 3rd law,

$$512 \quad M_{\text{sys}} = (4\pi^2 a^3)/(GP^2)$$

513 where a and P are the pre-impact semimajor axis and orbit period, and G is the gravitational
514 constant. Neglecting the aspherical shapes of Didymos and Dimorphos and their associated
515 gravitational potentials may lead to an overestimate of the system mass by $\sim 1\text{-}2\%$ ⁴⁸. However,
516 this error is negligible as the uncertainty in Dimorphos’s semimajor axis dominates the
517 uncertainty in the system mass. Next, the bulk density of the combined system was obtained by
518 dividing the system mass with the combined volume of both bodies,

$$519 \quad \rho_{\text{sys}} = (3M_{\text{sys}})/(4\pi[R_A^3 + R_B^3])$$

520 where R_A and R_B are the respective volume-equivalent radii of Didymos and Dimorphos. Based
521 on the pre-impact orbit period and semimajor axis⁶, and the volume-equivalent diameters
522 provided in this work, we calculated a nominal system bulk density of $2400 \pm 250 \text{ kg/m}^3$ using
523 the uncertainties quoted in the previous sentence. However, in order to represent additional
524 possible systematic uncertainties, we adopted a slightly larger uncertainty, which gives a system
525 bulk density of $2400 \pm 300 \text{ kg/m}^3$.

526 The porosity of Dimorphos was estimated as follows:

$$527 \quad \phi = 1 - (\rho_{\text{bulk}} / \rho_{\text{grain}})$$

528 In this work, we assumed that Dimorphos's bulk density matches the entire system's bulk
529 density. There are three NEA systems for which the satellite's bulk density has been
530 independently measured: 66391 Moshup, 2000 DP107, and 2001 SN263 (two satellites). Two of
531 those satellites (Squannit and 2001 SN263 gamma) were measured to be denser than the primary
532 and two were less dense (2001 SN263 beta and 2000 DP107 beta)²⁰⁻²². For all three systems, the
533 1-sigma uncertainties for the satellite and the primary densities overlap. Furthermore, recent
534 work⁴⁹ estimated that the size of Squannit is about 30% larger than estimated previously²⁰,
535 meaning that the bulk density of Squannit may be in better agreement with its primary. Given
536 these other examples, assuming Dimorphos's density matches the system bulk density is a
537 reasonable starting point, although its true density could differ significantly from this value. Hera
538 will determine the masses and densities of Didymos and Dimorphos and test the validity of this
539 assumption³⁹.

540

541 **Methods references**

542 40. Gaskell, R. W. *et al.* Characterizing and navigating small bodies with imaging data. *Meteorit.*
543 *Planet. Sci.* **43**, 1049–1061 (2008).

544 41. Barnouin, O. S. *et al.* Digital terrain mapping by the OSIRIS-REx mission. *Planet. Space Sci.*
545 **180**, 104764 (2020).

546 42. Palmer, E. E. *et al.* Practical Stereophotoclinometry for Modeling Shape and Topography on
547 Planetary Missions. *Planet. Sci. J.* **3**, 102 (2022).

- 548 43. Daly, R. T. *et al.* Shape Modeling of Dimorphos for the Double Asteroid Redirection Test
549 (DART). *Planet. Sci. J.* **3**, 207 (2022).
- 550 44. Al Asad, M. M. *et al.* Validation of Stereophotoclinometric Shape Models of Asteroid
551 (101955) Bennu during the OSIRIS-REx Mission. *Planet. Sci. J.* **2**, 82 (2021).
- 552 45. Barnouin-Jha, O. S. *et al.* Small-scale topography of 25143 Itokawa from the Hayabusa laser
553 altimeter. *Icarus* **198**, 108–124 (2008).
- 554 46. Burke, K. N. *et al.* Particle Size-Frequency Distributions of the OSIRIS-REx Candidate Sample
555 Sites on Asteroid (101955) Bennu. *Remote Sens.* **13**, 1315 (2021).
- 556 47. Pajola, M. *et al.* Size-frequency distribution of boulders ≥ 7 m on comet 67P/Churyumov-
557 Gerasimenko. *Astron. Astrophys.* **583**, A37 (2015).
- 558 48. Agrusa, H. F. *et al.* The excited spin state of Dimorphos resulting from the DART impact.
559 *Icarus* **370**, 114624 (2021).
- 560 49. Scheirich, P. *et al.* A satellite orbit drift in binary near-Earth asteroids (66391) 1999 KW4 and
561 (88710) 2001 SL9 — Indication of the BYORP effect. *Icarus* **360**, 114321 (2021).

562

563 **Extended data figures**

564 **Extended Data Fig. 1. The Dimorphos global digital terrain model (DTM) as viewed along**
565 **its principal axes.** The black star marks the DART impact site. Colors on the DTM indicate the
566 various constraints used to build the model.

567

568 **Extended Data Fig. 2. Tilts and topography at the impact site.** DTM of the DART impact site
569 with facets colored by the impact angle with respect to local horizontal, averaged over a 3-m
570 region. The DTM is lit to match the lightning in DRACO images at the time of impact. The

571 white circle shows the uncertainty in the impact location (a circle with a radius of 68 cm).
572 Boulders 1 and 2 correspond to boulders 1 and 2 in Figure 2. (b) The same DTM with DRACO
573 image `dart_0401930048_45552_01_iof.fits` draped over it. The image does not cover the entire
574 DTM, so the corners of panel b show the impact angle plate coloring. (c) Histogram of tilts
575 within the white circle representing the uncertainty in the impact site location. (d) – (g)
576 Perspective views of the impact site DTM with overlaid image shown in (b), i.e., the DTM in
577 panel (b) viewed edge on from each of the four sides of the DTM. Boulders 1 and 2 are
578 prominent, as is the small niche between them in which the spacecraft bus hit the surface.

579

580 **Extended Data Fig. 3. Boulders at the impact site.** (a) Zoomed-in view of the impact site
581 DTM to focus on the two largest boulders near the impact site. Facets in the DTM are colored by
582 the height of the facet along a normal to a plane fit to all of the points in the DTM. DRACO
583 image `dart_0401930048_45552_01_iof.fits` is draped over the DTM at 40% opacity. The DTM is
584 lit to match the lightning in the DRACO image. The white circle shows the uncertainty in the
585 impact location (a circle with a radius of 68 cm). The red and blue paths show the locations of
586 two topographic profiles across (b) boulder 1 from A to A' and (c) boulder 2 from B to B'.

587

588 **Extended Data Fig. 4. Dimorphos and Didymos as seen by DART.** (a) The asteroid
589 Dimorphos seen at a range of pixel scales. Numerous boulders can be distinguished across the
590 surface in images as coarse as 2–3 m pixel scale. Without the context of higher-resolution
591 images, it would be difficult to definitively identify boulders in the 4-m pixel scale image. Image
592 names (from left to right): `dart_0401929985_18096_01_iof.fits`,
593 `dart_0401929952_31226_01_iof.fits`, `dart_0401929919_44355_01_iof.fits`. (b) Composite image

594 of asteroids Dimorphos and Didymos. Dimorphos is at left; Didymos is at right. The two
595 asteroids and the distance between them are to scale. This image was produced by combining
596 two DRACO images to show Dimorphos at higher resolution than Didymos. In spite of the
597 different resolutions, the two surfaces give different first impressions. Dimorphos has a boulder-
598 rich surface with an ellipsoidal shape. Didymos exhibits boulders but also smoother areas and
599 larger concavities. The north poles of Dimorphos and Didymos point to the top of the figure.

600

601 **Extended Data Fig. 5. The final full DRACO image of Dimorphos's surface.** Examples of
602 cracks (white arrows), rocks on rocks (squares) and a partially buried boulder are indicated.
603 Image name: dart_0401930049_43695_01_iof.fits. The north pole of Dimorphos is toward the
604 top of the figure.

605

606 **Extended Data Fig. 6. The size-frequency distribution of boulders identified in the last**
607 **DRACO full image** (dart_0401930049_43695_01_iof.fits). The limit of image resolution,
608 assuming ≥ 3 pixel sampling, is ~ 16.5 cm, so the overturn at small sizes is real and not an
609 observational bias (Pajola et al. 2015). Here, a conservative 5-pixel sampling limit (27.5 cm) is
610 indicated by the vertical blue dashed line. The distribution is not well described by a single
611 power law (shown here as a red dot-dashed line with a slope of -1.65).

612

613 **Extended Data Fig. 7. Shape modeling process used to build a global digital terrain model**
614 **of Dimorphos.** The process was informed by shape modeling tests conducted prior to impact.

615

616 **Extended Data Fig. 8. Sunlit and Didymos-lit limbs of Dimorphos.** The same image of
617 Dimorphos stretched to optimize (a) the limb lit by the Sun and (b) the limb lit by light reflected
618 off Didymos. In (b), pixels with $I/F < 0.014$ have been scaled up by a factor of 6 to allow the
619 faint features to be seen along with the sunlit features, for better comparison to (a). Together, the
620 two limbs reveal a complete outline of the asteroid as seen by DRACO. The image is
621 `dart_0401930039_14119_01_iof.fits`.

622
623 **Extended Data Fig. 9. Shape model assessments.** (a) – (e) show results from limb/terminator
624 shape model assessments. Panels (a) – (c) show an example of (a) a reference DRACO image,
625 (b) the rendered shape model with the same lighting and viewing geometry as the reference
626 image, and (c) the difference between the model and the reference image. (d) and (e) show
627 results from limb/terminator assessments from many DRACO images. (d) Sum of the absolute
628 value of the image-model differences, normalized by the image perimeter. The median is the
629 most relevant measure of uncertainty from this metric because the distribution is always one-
630 sided and never gaussian. (e) The differences in the radii of the equivalent-area circles for the
631 reference image and rendered shape model, respectively. The radius of the equivalent-area circle
632 is the radius of a circle with the same area as the total area of lit terrain on either the rendered
633 model or the reference image. The mean is the most relevant measure of uncertainty from this
634 metric because the distribution should be symmetric. (f) – (i) show results from keypoint
635 assessments. The colored lines in panels (f) and (g) connect features matched by the algorithm in
636 the image and on the shape model. Most, but not all, matches are reasonable, so the median value
637 based on all keypoints is used. (h) shows a metric derived from differences between
638 corresponding keypoints across several tens of DRACO images. (i) shows a model-to-image

639 scale factor derived by comparing the distances measured between all keypoints in the reference
640 DRACO image to the distances measured between all keypoints in images of the rendered shape
641 model. The arrows in panels (a) and (g) indicate the direction of Dimorphos north (+Z).

642

643 **Extended Data Fig. 10. Fit residuals.** (a) Spacecraft position residuals and (b) residual
644 distributions estimated after fitting the spacecraft locations obtained during the SPC shape
645 modeling process with a second-order polynomial all in the J2000 inertial frame relative to
646 Dimorphos. Uncertainties attributed to the location of the impact site and reported in Table 1 are
647 in the Y and Z axes.

648

649 **Data availability**

650 The DRACO images shown in this paper, the global digital terrain model of Dimorphos, and the
651 local digital terrain model of the impact site are available in a permanent archive associated with
652 this paper in the JHU/APL Data Archive ([https://lib.jhuapl.edu/papers/dart-an-autonomous-
653 kinetic-impact-into-a-near-earth/](https://lib.jhuapl.edu/papers/dart-an-autonomous-kinetic-impact-into-a-near-earth/)). All raw and calibrated DRACO images, as well as higher-order
654 products such as digital terrain models, will ultimately be available via the Planetary Data
655 System (PDS) (https://pds-smallbodies.astro.umd.edu/data_sb/missions/dart/index.shtml) by
656 October 2023.

657 **Acknowledgements**

658 We thank Paul Boie, Ray Harvey, Mark Hill, Andrew Johnson, Cindy Kim, Jong Kim, Daniel
659 O'Shaughnessy, Nadja Osiander, Geoffrey Ottman, Lev Rodovskiy, Matthew Rodriguez, Andrew
660 Smith, Kirk Volland, and all of the other people who made the DART impact possible. We thank

661 Megan Bruck Syal and Kathryn Kumamoto for their feedback on the manuscript. This work
662 made use of the Small Body Mapping Tool.
663
664 This work was supported by the DART mission, NASA Contract No. 80MSFC20D0004. This
665 work was supported by the Italian Space Agency (ASI) within the LICIACube project (ASI-
666 INAF agreement AC n. 2019-31-HH.0). P.S. and P.P. were supported by the Grant Agency of
667 the Czech Republic, grant 20-04431S. B.J.B. was funded by the NASA DART Participating
668 Scientist Program #20-DARTPSP20-0007. S.C. acknowledges funding from the Crosby
669 Distinguished Postdoctoral Fellowship Program of the Department of Earth, Atmospheric and
670 Planetary Science, Massachusetts Institute of Technology. G.S.C. was funded by UK Science
671 and Technology Facilities Council Grant ST/S000615/1. F.F. acknowledges funding from the
672 Swiss National Science Foundation (SNSF) Ambizione grant No. 193346. M.J. and S.D.R.
673 acknowledge support by the Swiss National Science Foundation (project number
674 200021_207359), and from the European Union's Horizon 2020 research and innovation
675 programme under grant agreement No. 870377 (project NEO-MAPP). T.K. is supported by
676 Academy of Finland project 335595 and by institutional support RVO 67985831 of the Institute
677 of Geology of the Czech Academy of Sciences. P.M. acknowledges funding support from the
678 European Union's Horizon 2020 research and innovation program under grant agreement No.
679 870377 (project NEO-MAPP), the CNRS through the MITI interdisciplinary programs, CNES
680 and ESA. N.M. and C.Q.R. acknowledge funding support from the European Commission's
681 Horizon 2020 research and innovation programme under grant agreement No 870377 (NEO-
682 MAPP project) and support from the Centre National d'Etudes Spatiales (CNES). J.O. has been
683 funded by grant No. PID2021-125883NB-C22 by the Spanish Ministry of Science and

684 Innovation/State Agency of Research MCIN/AEI/ 10.13039/501100011033 and by “ERDF A
685 way of making Europe”. S.R.S. acknowledges support from the NASA DART Participating
686 Scientist Program, award no. 80NSSC22K0318. J.K.S. acknowledges support from NASA award
687 80NSSC21K1014. J.M.T.-R. acknowledges financial support from the Ministerio de Ciencia e
688 Innovación—Agencia Estatal de Investigación (PID2021-128062NB-I00). P.B. acknowledges
689 funding support from Europlanet/University of Edinburgh and Technical University of Kenya.
690 Part of this research was carried out at the Jet Propulsion Laboratory, California Institute of
691 Technology, under a contract with the National Aeronautics and Space Administration.

692

693 **Author contributions**

694 R.T.D., C.M.E., and O.S.B. jointly led the writing of this paper, identification of the impact site,
695 and shape modeling of Dimorphos. R.T.D is the Dimorphos shape modeling lead. C.M.E. is the
696 DRACO instrument scientist. O.S.B. is the Proximity Operations Working Group lead. N.L.C.,
697 A.S.R. and A.F.C. lead the DART Investigation Team, contributed to writing and revision of this
698 paper, and coordinated inputs across the DART Investigation Team. E.Y.A. contributed
699 substantial revisions to the manuscript and was the DART mission systems engineer. H.F.A.
700 wrote portions of the manuscript and played a key role in the analysis and interpretation of
701 DART data. E.D.A., A.L.A., J.A.A., A.R.B., D.L.B., J.B., S.B., M.H.C., G.C., M.W.C., P.S.E.,
702 A.S.F., Z.J.F., S.H., M.A.H., P.A.H.-D., P.M.H., S.N.J., M.A.J., J.W.J., T.O.K., F.E.L., D.M.M.,
703 M.E.M., I.W.M., J.R.R., E.L.R., J.E.R., L.M.Rodriguez, L.M.Roufberg, B.P.R., C.A.S., M.P.S.,
704 B.N.S., C.E.S., E.J.S., E.A.S., Z.B.T., J.R.T., B.T.T., A.T.V., D.V., D.S.W., and K.A.W. played
705 integral roles in the engineering team to ensure DART intercepted Dimorphos. R.W.G., M.A.J.,
706 and H.N. contributed to the effort to identify the impact site. R.W.G. also assisted with shape

707 modeling of Dimorphos. E.E.P. led the efforts to use DRACO images to determine the shape of
708 Didymos, with inputs from O.S.B., and R.W.G. B.J.B. calculated the geometric albedo of
709 Didymos. T.L.F. contributed to the calibration of DRACO and shape modeling efforts. D.S.W.
710 led determination of the time of impact and wrote that part of the methods section. R.C.E., H.N.,
711 and C.D.W. developed the software used to process DRACO images and digital terrain models
712 into data products. S.-Y.W.H. contributed to DRACO calibration. A.L., N.M., M.P., S.D.R.,
713 C.Q.R., A.M.S., D.M.G., M.E.D., and J.M.S. contributed to impact site characterization. T.K.,
714 H.F.A., M.C.N., D.J.S., J.M.T.-R., Y.Z. contributed to the calculation and interpretation of the
715 density of Dimorphos. S.R.C., N.A.M., S.P.N., C.A.T., P.P., and P.S. provided orbit solutions
716 used to compute the GM of the Didymos system. E.I.A., P.B., R.-L.B., S.C., G.S.C., F.F.,
717 D.M.G., I.H. M.H., S.A.J., M.J., R.L., P.M., S.M., M.C.N., J.O., K.T.R., D.J.S., S.R.S, and
718 J.K.S. provided comments that substantively revised the manuscript. This work made use of the
719 Small Body Mapping Tool (SBMT; sbmt.jhuapl.edu). R.J.S., J.M.P., and N.R.L. are the software
720 developers for the SBMT. C.M.E., O.S.B., R.T.D., and A.C.M. also work on the SBMT team.

721

722 **Competing interests**

723 The authors declare no competing interests

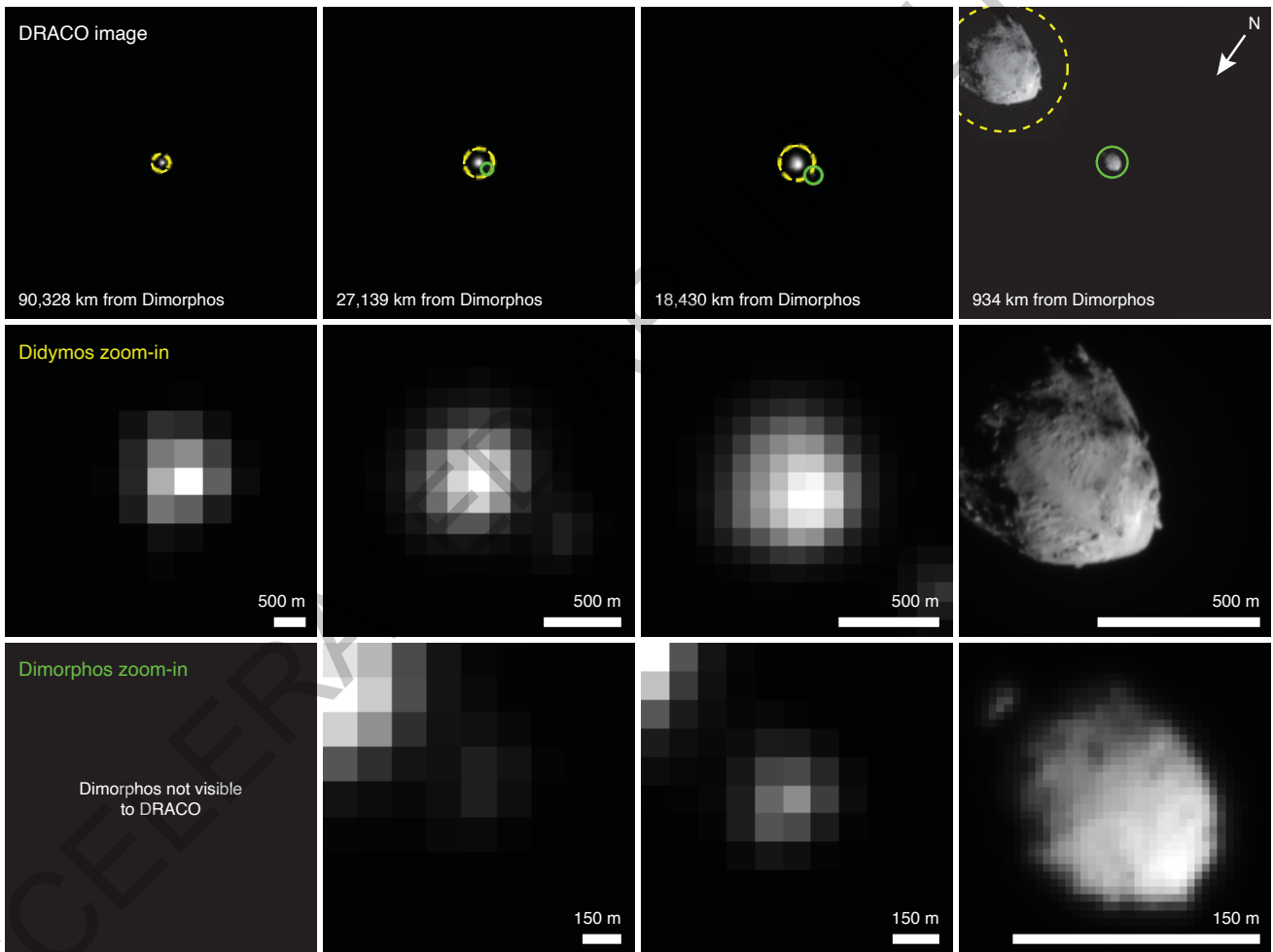
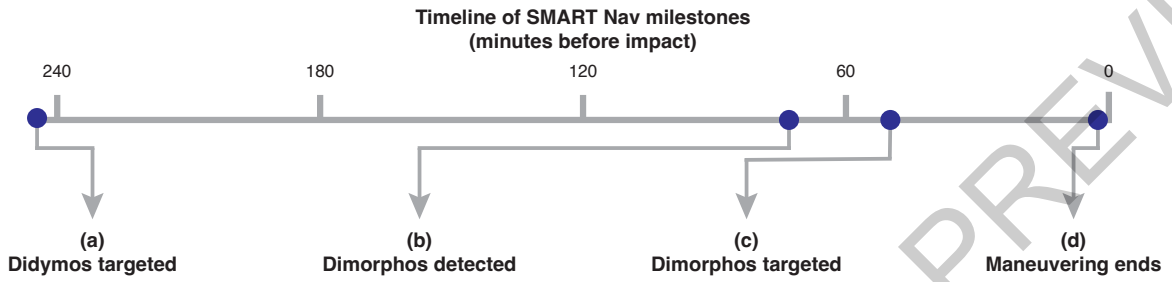
724

725 **Additional information**

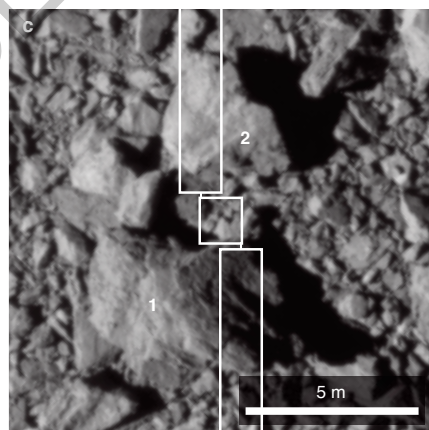
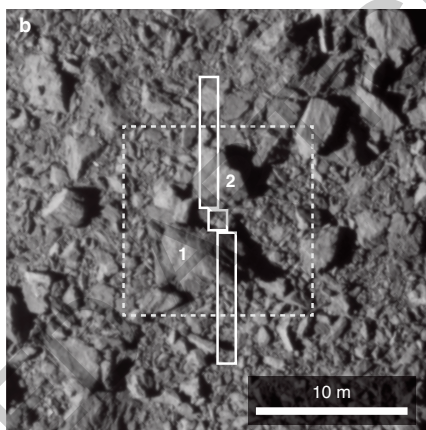
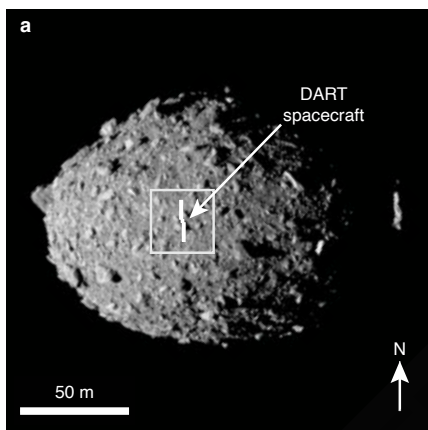
726 Correspondence and requests for materials should be addressed to Dr. Terik Daly

727 (terik.daly@jhuapl.edu).

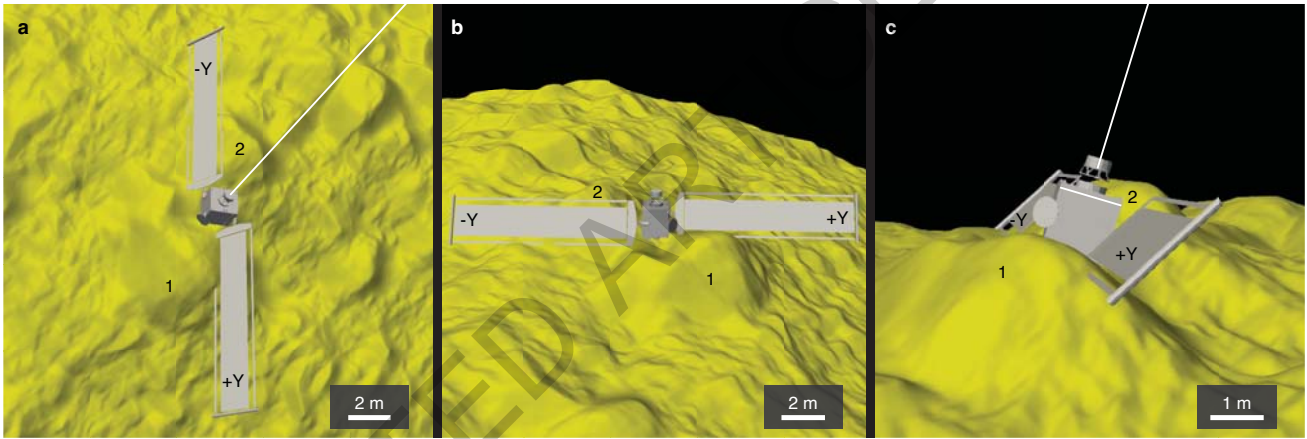
728

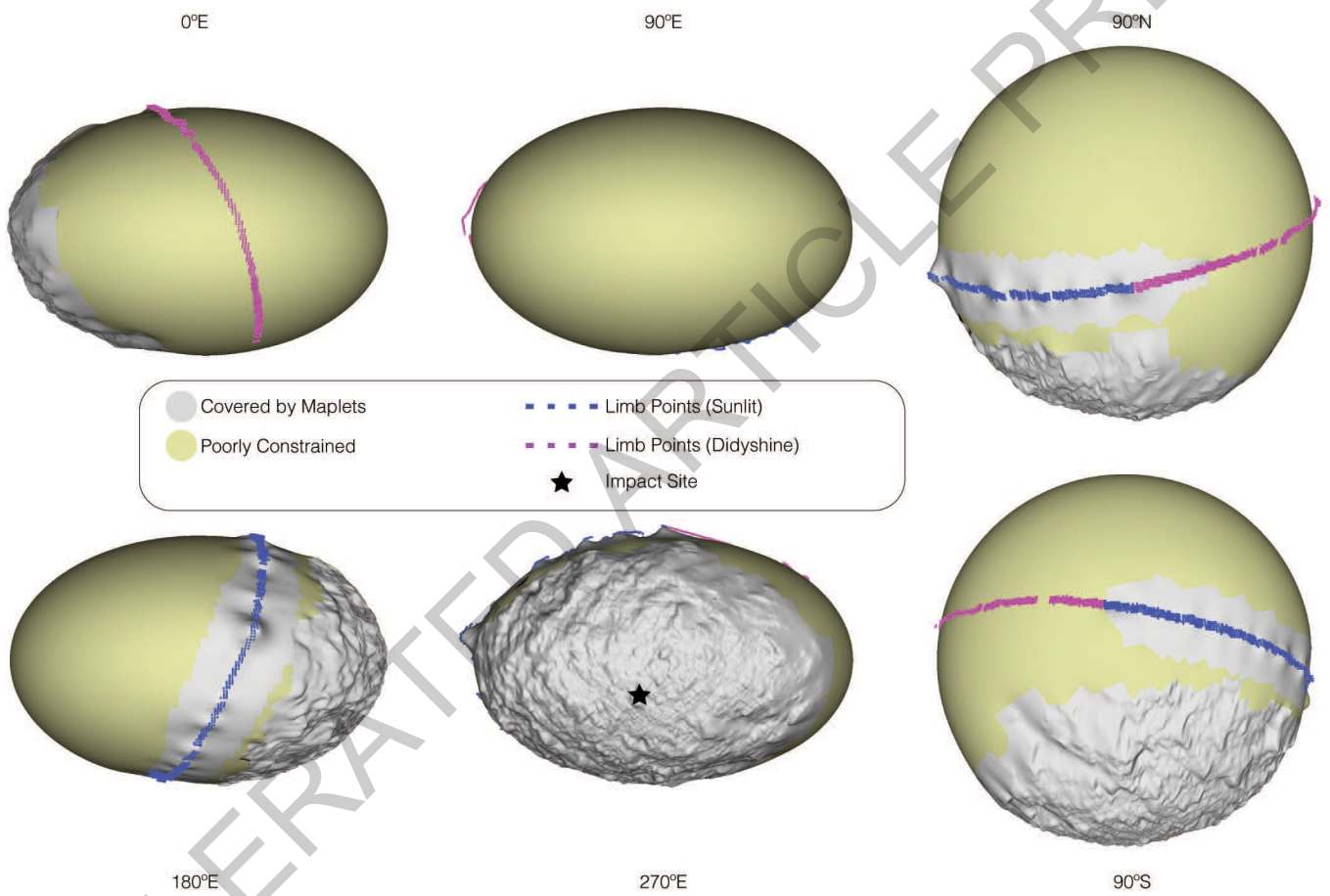


ACCELERATING THE FUTURE OF SPACE EXPLORATION

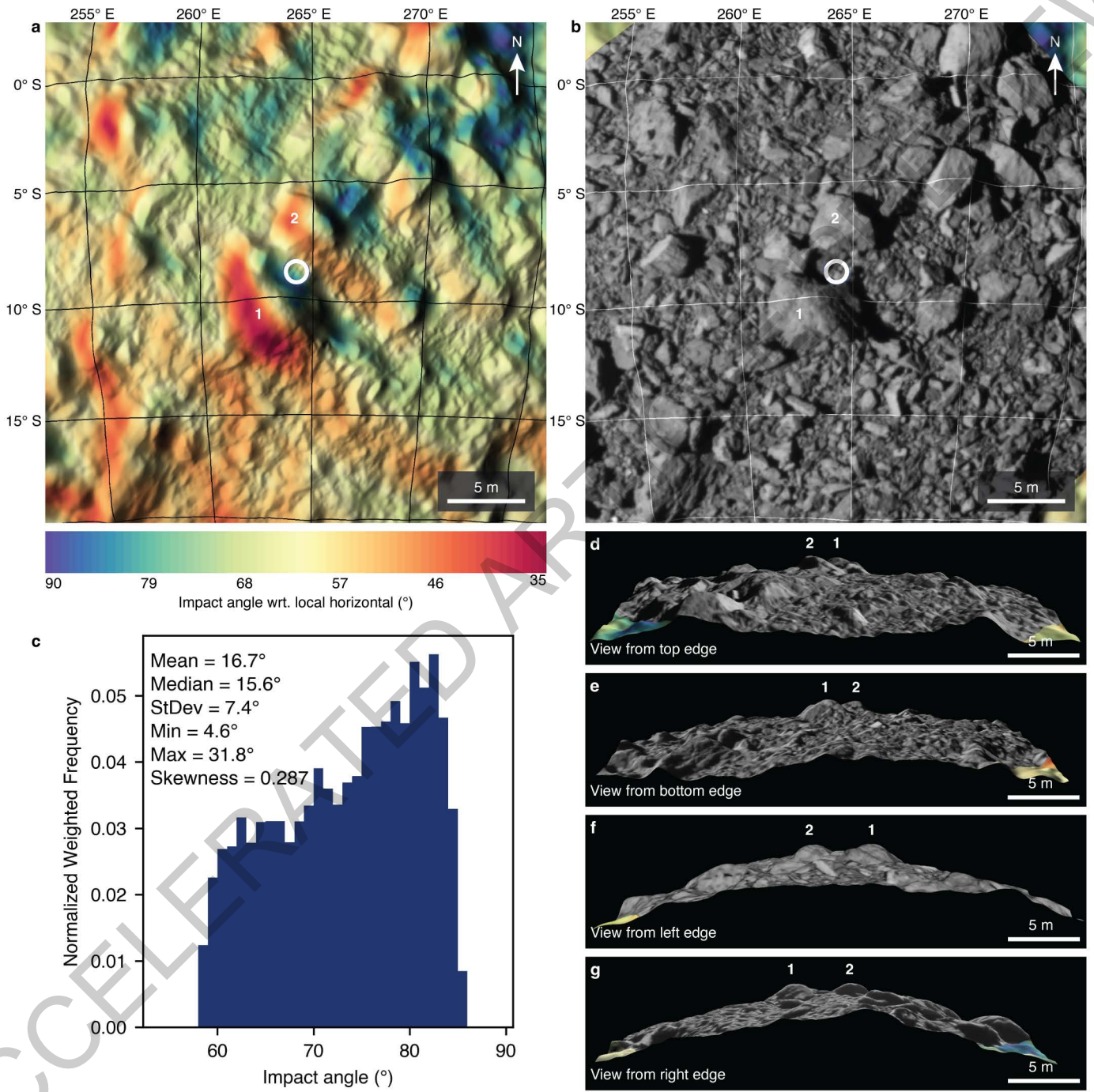


ACCELERATED RELEASE PREVIEW

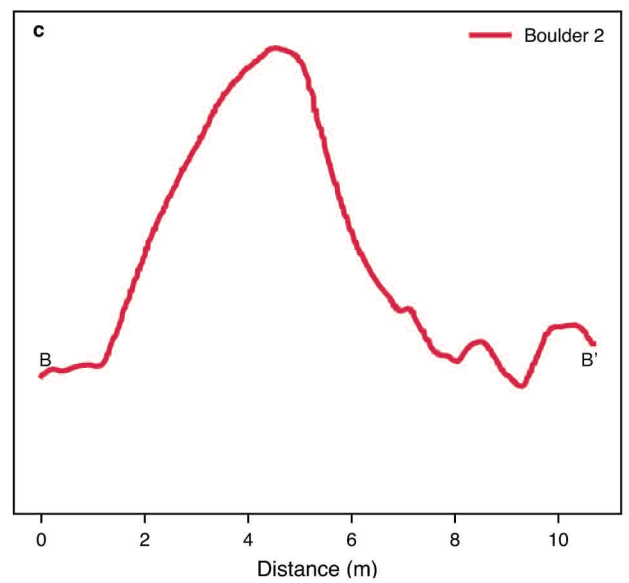
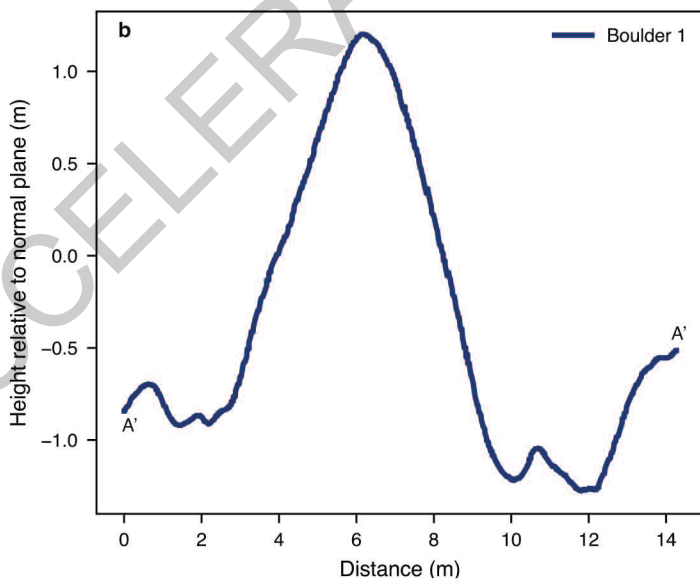
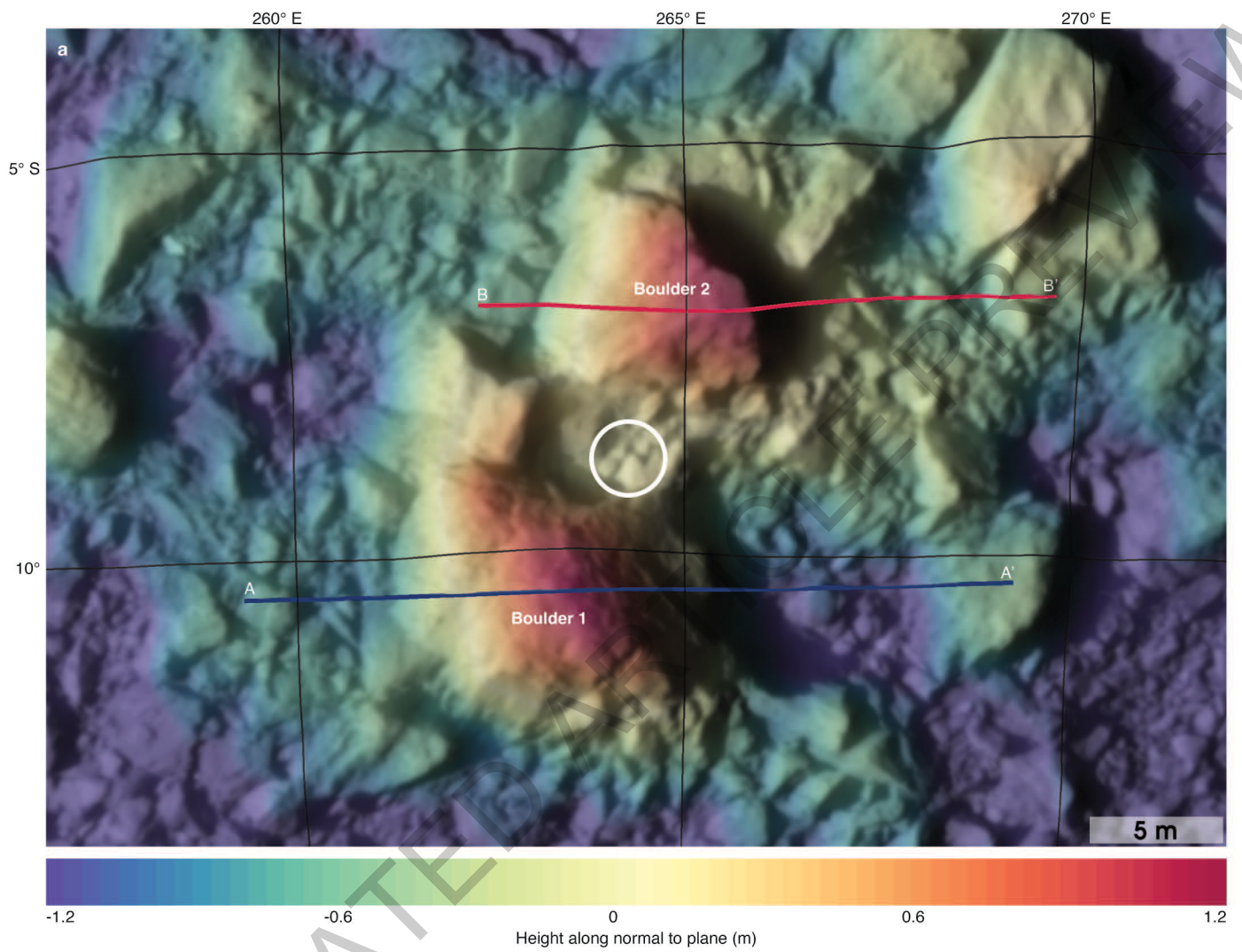




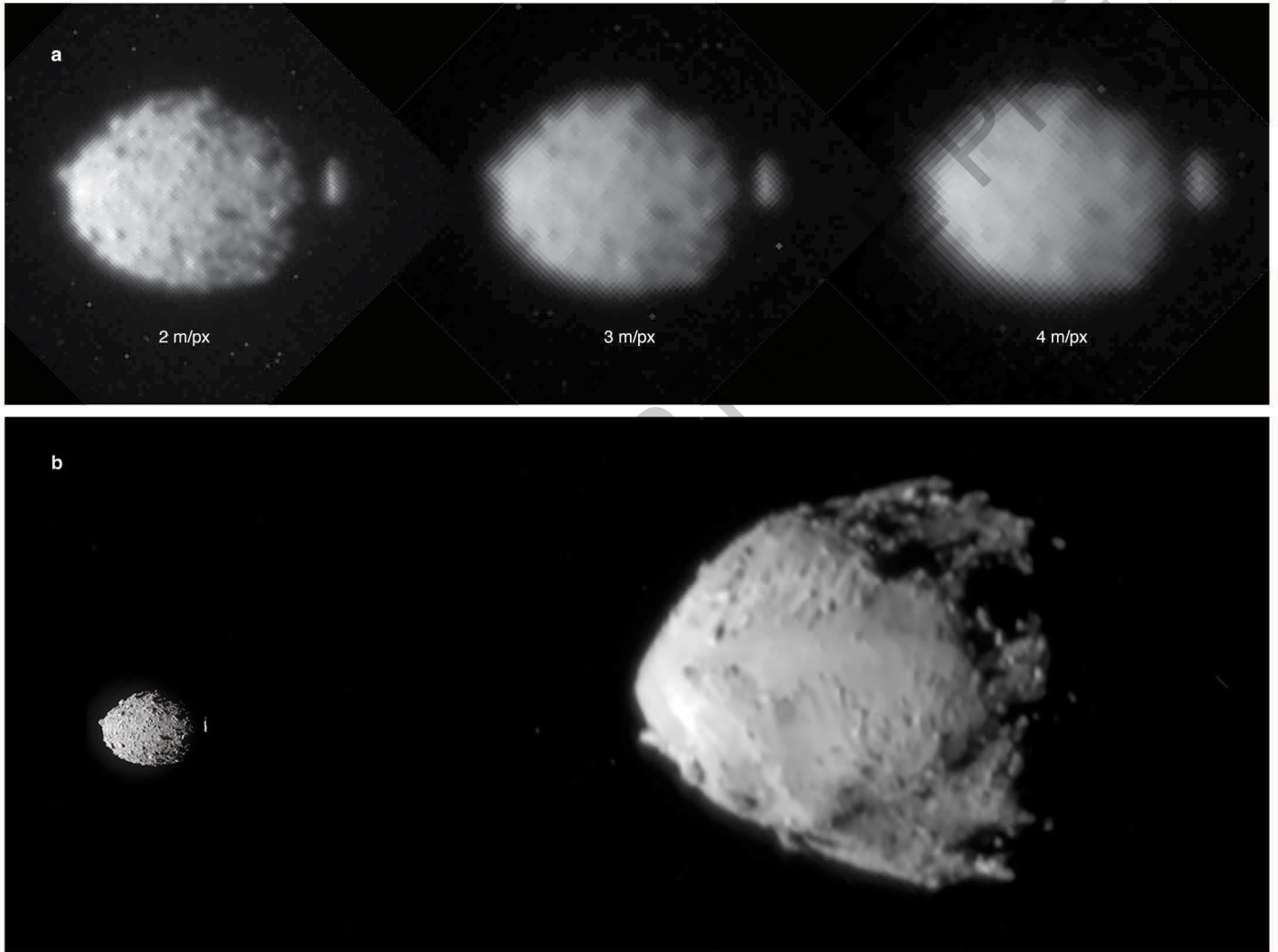
Extended Data Fig. 1



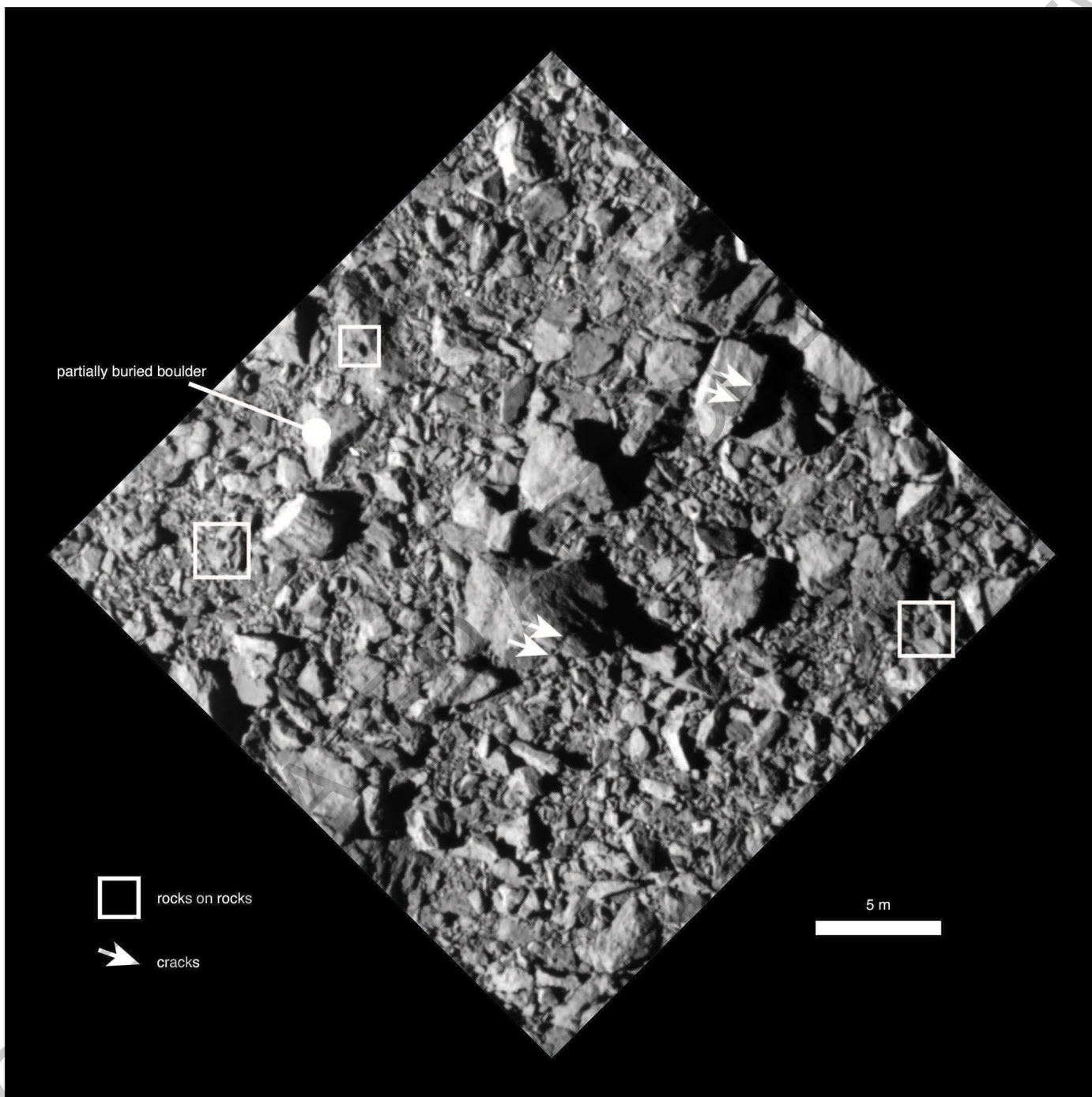
Extended Data Fig. 2



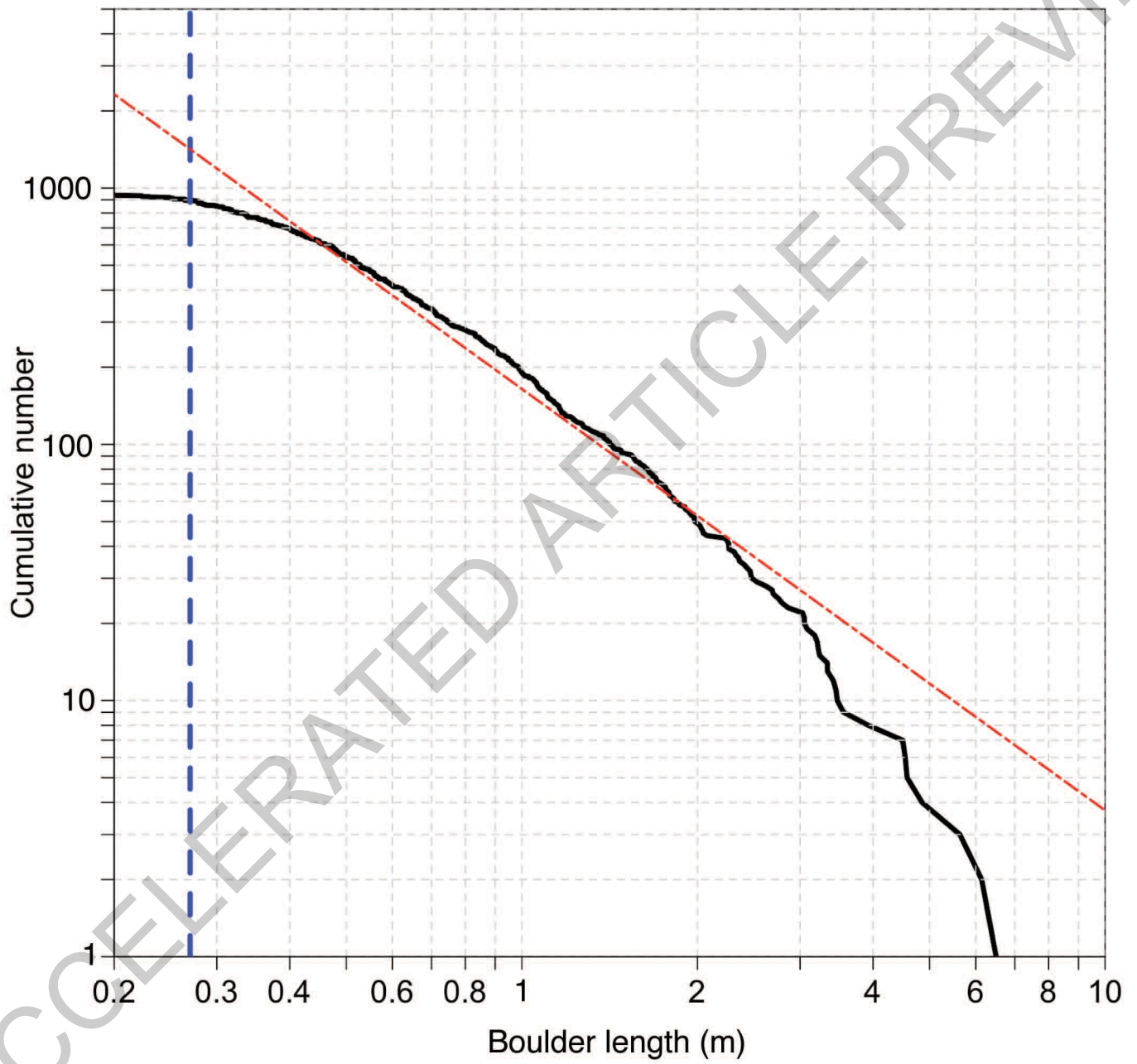
Extended Data Fig. 3



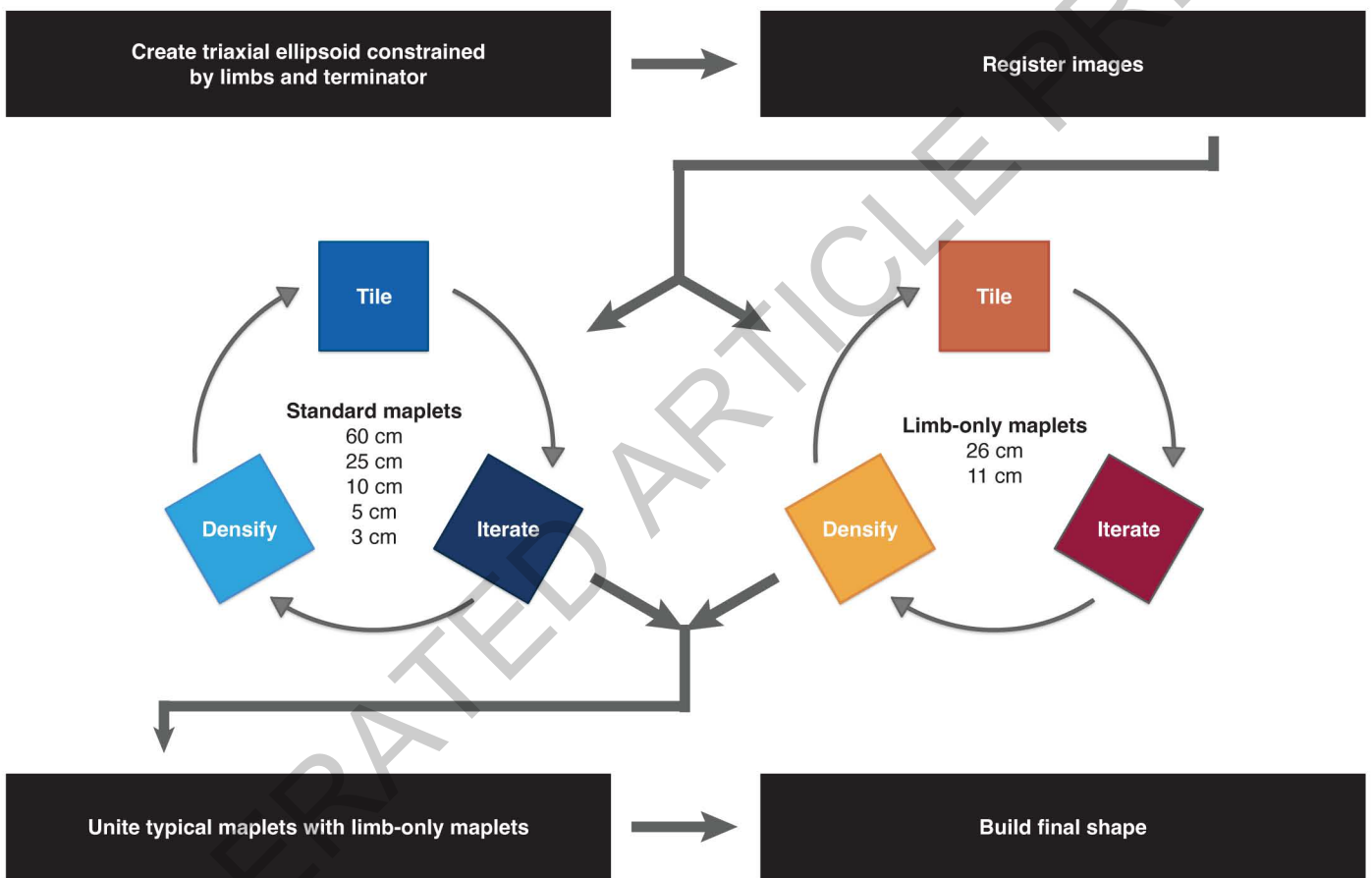
Extended Data Fig. 4



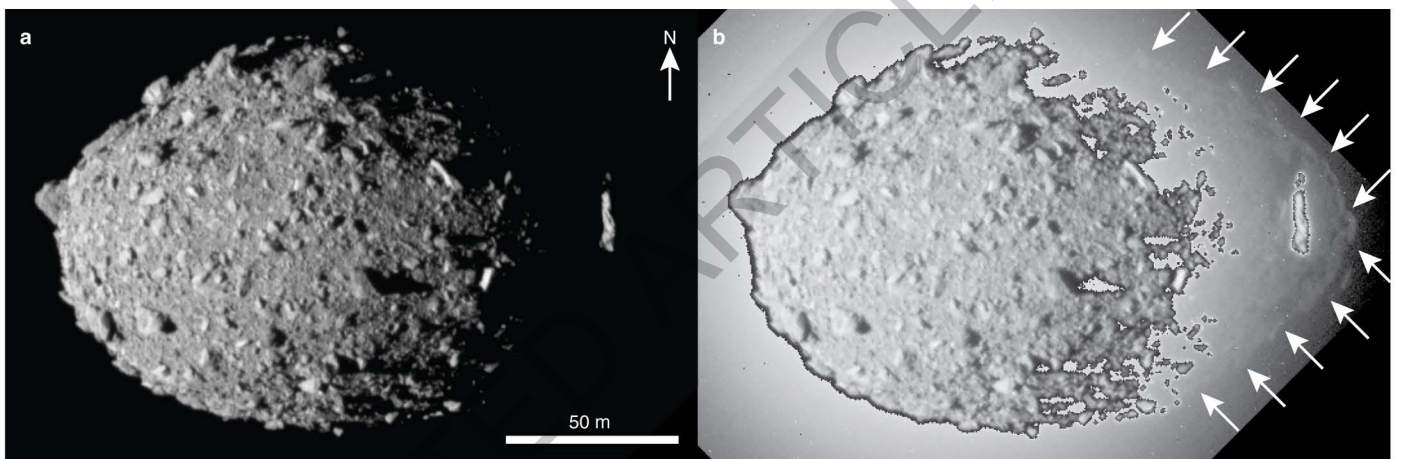
Extended Data Fig. 5



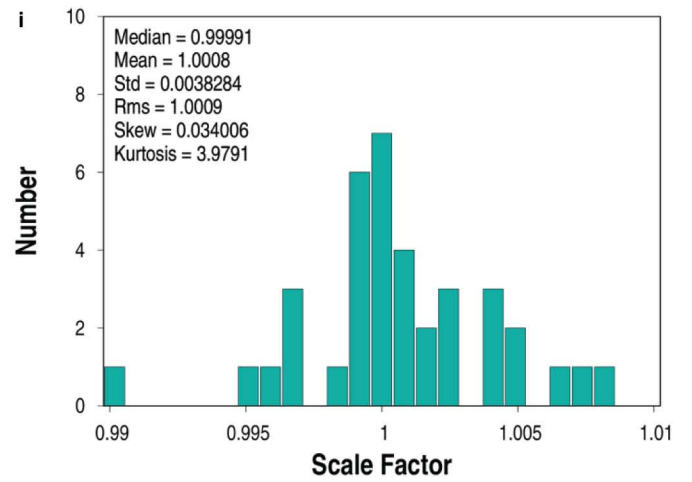
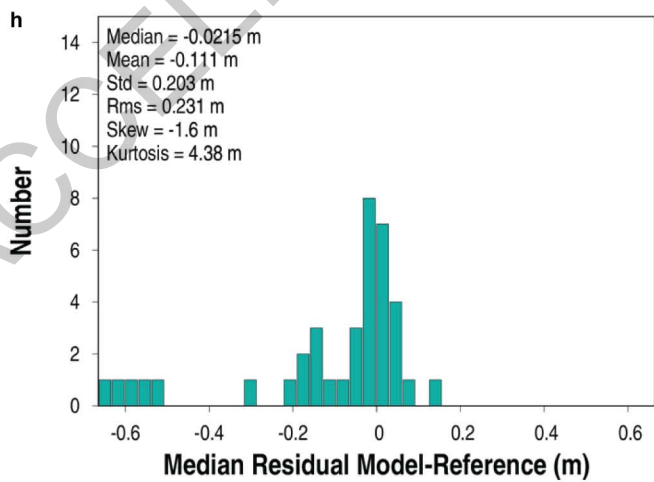
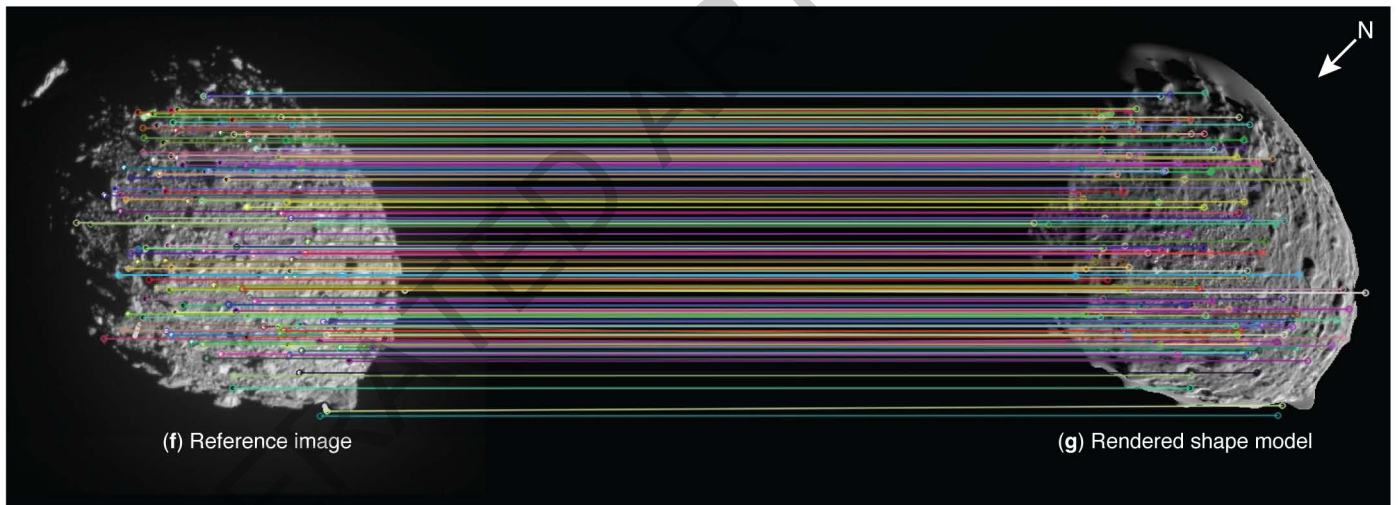
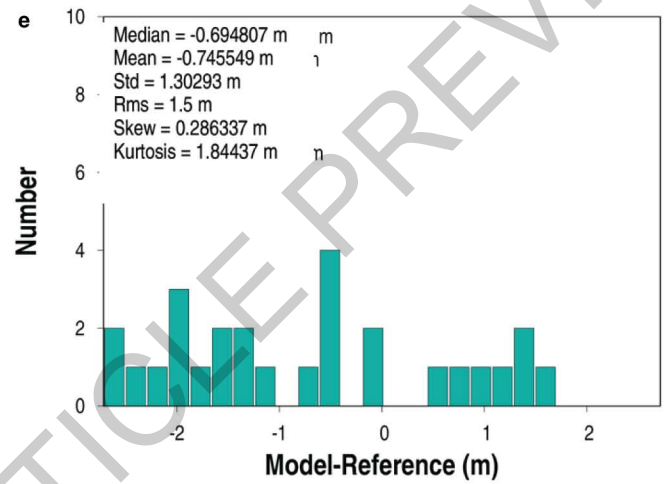
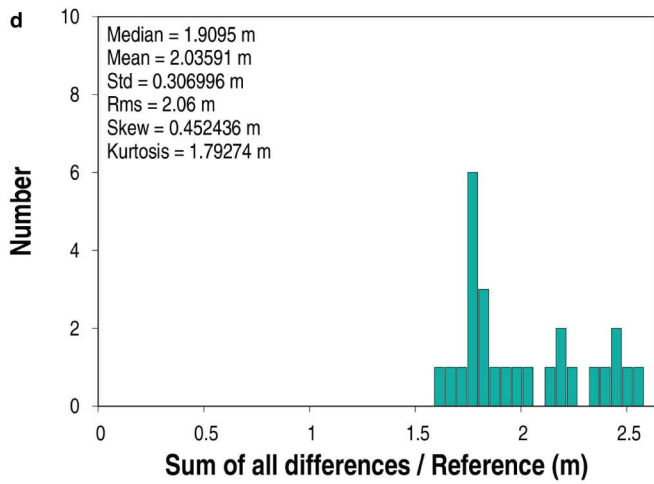
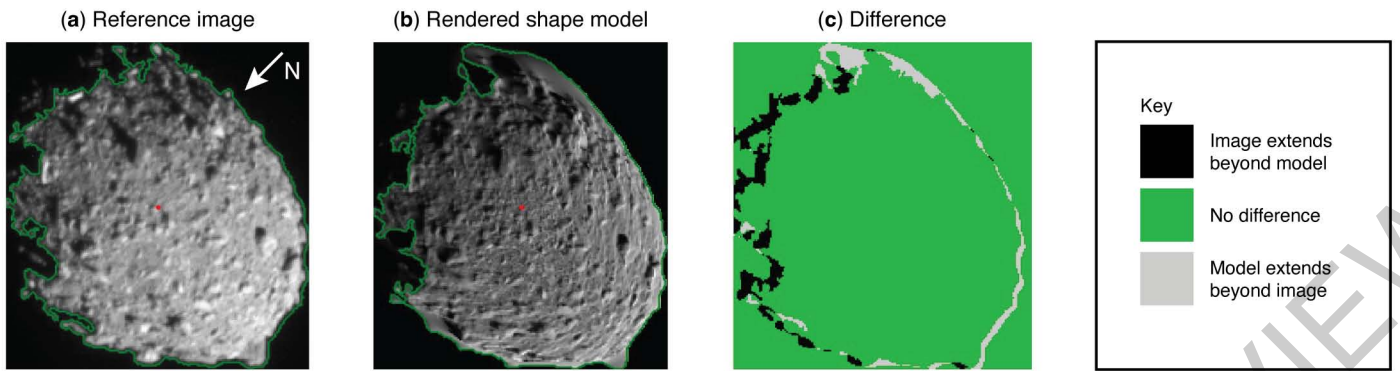
Extended Data Fig. 6



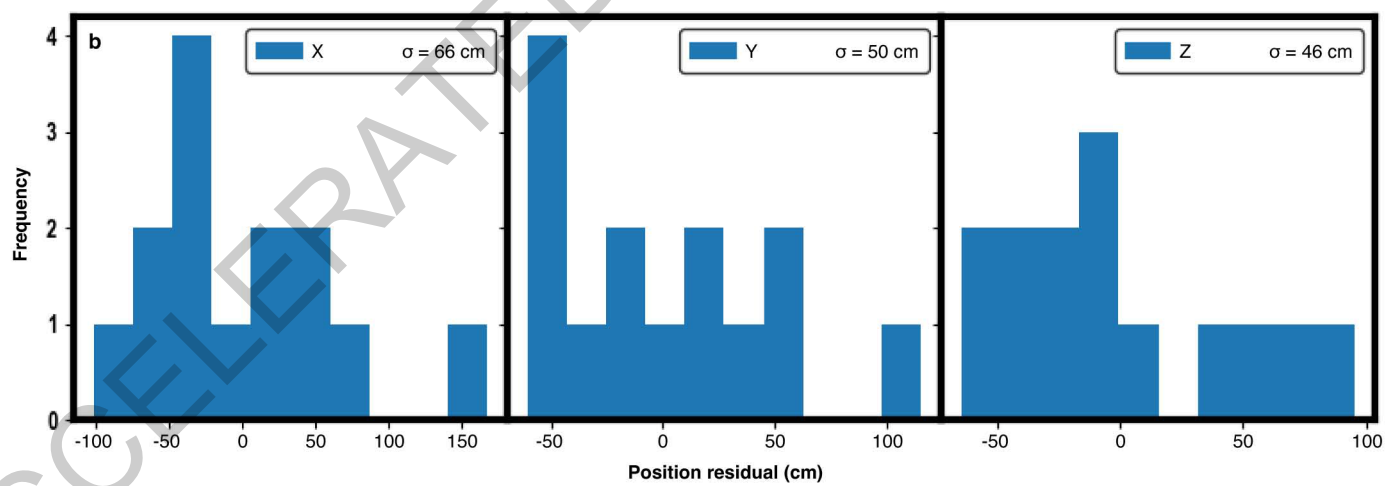
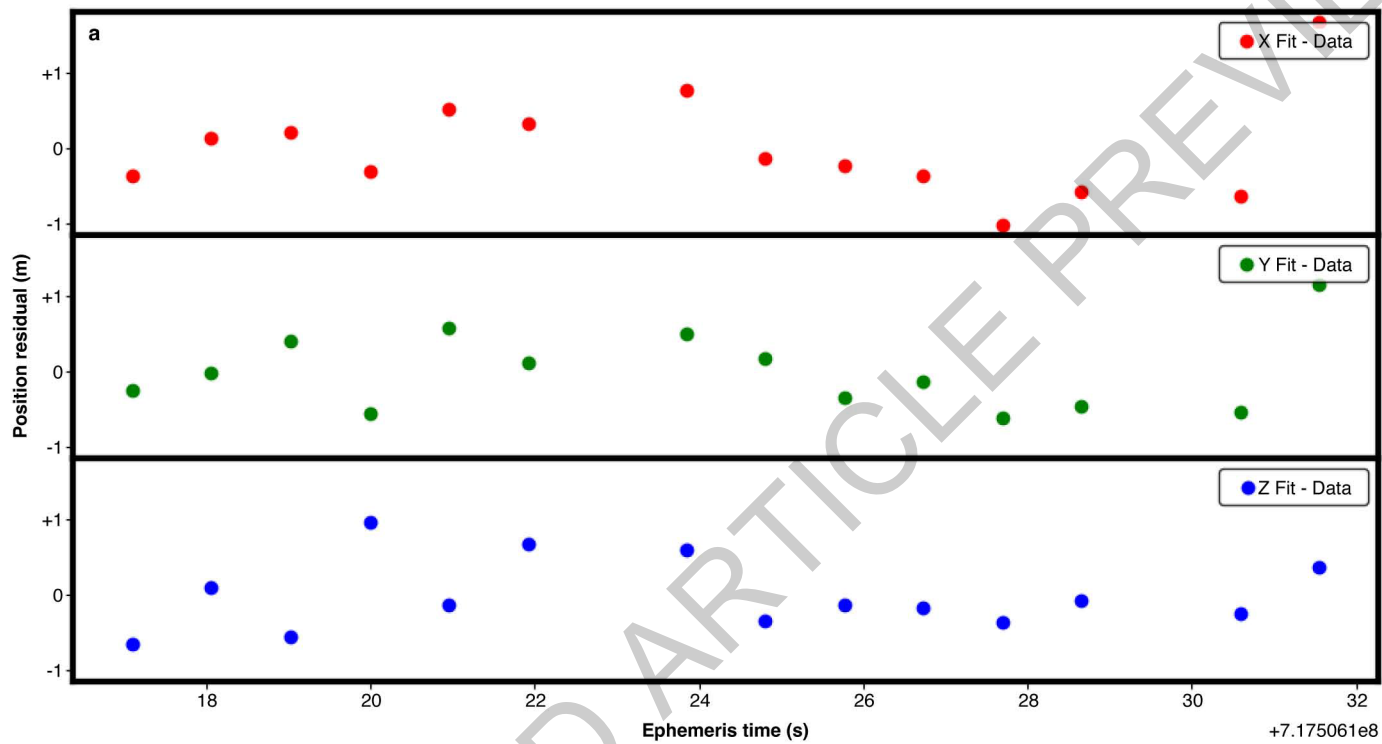
Extended Data Fig. 7



Extended Data Fig. 8



Extended Data Fig. 9



Extended Data Fig. 10